Performance evaluation of multipinhole μSPECT systems for short time frames

Georgios Vranas

Master of Science Thesis

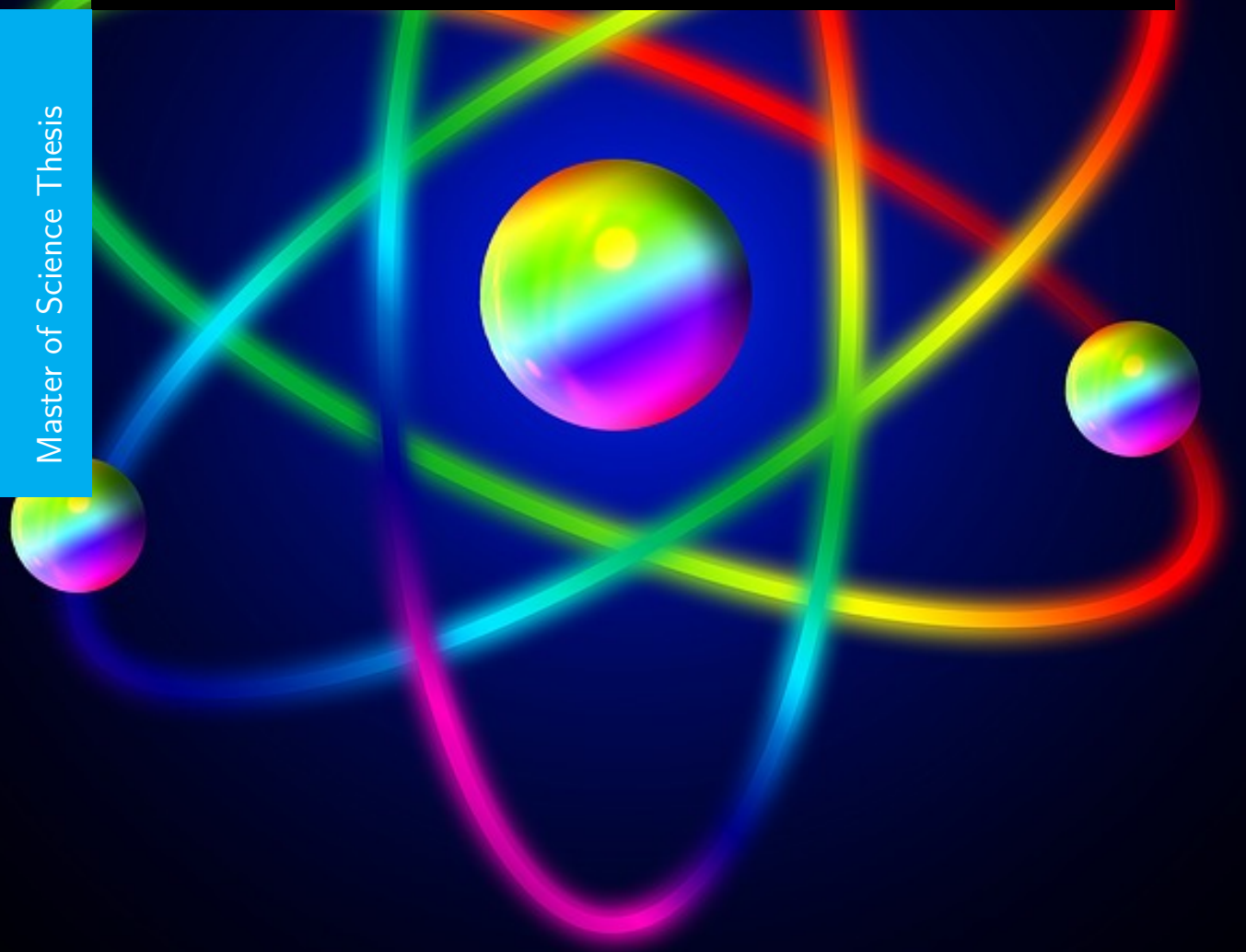

TU Delft Delft University of Technology

MSc Biomedical Engineering

Performance evaluation of multipinhole μSPECT systems for short time frames

Georgios Vranas

in partial fulfilment of the requirements of the degree

Master of Science
in Biomedical Engineering

at Delft University of Technology,
to be defended publicly on Monday November 27, 2017 at 10.00am

Supervisor: Dr.ir. D.R. Schaart
Thesis committee:
Dr. ir. M.C. Goorden (TU Delft)
Dr. ir. A.G. Denkova (TU Delft)
Dr. M. Bernsen (Erasmus MC)
Ir. M. Segbers (Erasmus MC)

Faculty of Mechanical, Maritime and Materials Engineering (3mE) · Delft University of Technology

Abstract

Purpose:
The need of image (frame) acquisitions within short time intervals is of major importance for preclinical SPECT imaging. The short frame times enable higher temporal resolution which is required in bio-distribution and pharmacokinetic studies where fast dynamic imaging is performed. The present study evaluates and compares the performance of two different preclinical multipinhole SPECT systems (NanoScan, VECTor) for short frames acquisitions.

Procedure (Materials & Methods)
Prior to the systems comparison, the comparison and selection of the best performing fast imaging mode provided by NanoScan system (Mediso) was performed. The fast imaging modes of this system provide acquisitions with 1,2 and 3 detector position around the animal bed. This comparison was performed by using uniform phantoms (syringes) and the rods of the NEMA NU4IQ phantom (frames: 6-30s). The down-sized version of NU4IQ phantom (SPECTIQ phantom) was used in this study to compare the performance of VECTor (MILabs) and NanoScan when performing acquisitions with short frame times (18s-600s, whole body scans). The quality of the acquired images was assessed in terms of absolute quantification (recovery coefficient), noise levels and visual evaluation.

Results:
The quantification with the NanoScan was accurate ($\pm 5\%$) regardless of times frames duration and activity concentrations when imaging large structures. The increase in number of detector positions yielded images with lower noise levels. In the case of small structures, acquisition with 3 detector positions (Semi-3 mode) appeared to provide more accurate activity recovery compared to acquisitions with 1 (stationary mode) and 2 detector positions (Semi-2 mode). Especially in the case of the 2mm diameter rod of the NU4IQ phantom, the Semi-3 mode appears to provide significantly more accurate activity recovery (30s frame). The systems comparison showed activity recovery with up to 5% deviation from the dose calibrator measurement when imaging the uniform region of SPECTIQ phantom (d = 21mm). Both systems could recover the three largest rods (d = 1.5, 1.0, 0.75mm) for the longest frames used(180,360,600s). None of the systems could recover the two smallest rods of the phantom (d=0.5,0.35mm). As the frame time decreased, both systems could recover less number of rods. VECTor appeared to provide higher activity recovery than NanoScan for the three

largest rods of the phantom. However, as the frame time decreased the differences became less significant. Furthermore, VECTor provided and 22.2% and 46.6% less spillover in air- and water-filled phantom regions (after reaching convergence) than NanoScan did.

Conclusions:
The performances of two preclinical SPECT systems (NanoScan, VECTor) for short time acquisitions were compared. The conducted experiments showed that the systems perform equally when conducting short frames imaging. Furthermore, the fast imaging mode of NanoScan employing three detector positions showed better performance than the other two fast imaging modes provided by this system.

Table of Contents

List of Figures

List of Tables

Chapter 1

Introduction

Single Photon Emission Computed Tomography (SPECT) has a prominent position in the field of molecular imaging. The aim of this scientific field is the study of molecular processes in order to understand disease and pharmacokinetic models with the possibility of direct translation of the results from preclinical laboratories to the human clinical setting. The main features of SPECT that justify its utility are the ability to image small molecules in picomolar concentrations and to quantify radioactive tracers injected into small animals. These capabilities contribute in the visualization and quantification of kinetic processes and physiological pathways in vivo (1). The imaging and quantification of the administered gamma-emitting tracers is performed non-invasively without the need of animal dissection (2). Furthermore, SPECT systems can perform simultaneous imaging of multiple molecular pathways by detecting radioisotopes with different gamma emission energies (3, 4). Due to the above-mentioned characteristics, small-animal SPECT has a significant role in various applications including disease studies, development of new radiopharmaceuticals, diagnostic tracers and therapeutic imaging (5–12). The large number of applications of preclinical SPECT in the field of molecular imaging is stimulating for further investment in research and development of this imaging modality.

Dynamic imaging is a technique where image acquisition is performed at multiple sequential time points resulting in a sequence of images (frames) within a specific time period. This imaging technique is performed in bio-distribution and pharmacokinetic studies in small animals in order to track the concentration time courses of injected radiotracers in the organs of interest. This is done by quantifying the temporal changes of radionuclide concentration in those organs between different frames. For this purpose, short frames are required to provide adequate temporal resolution, resulting in better understanding of the pharmacokinetic processes. It is of great importance for a dynamic imaging study to have sufficient temporal resolution due to the tracers' rapid clearance from the organs of interest.

Recent technological developments in high sensitivity preclinical SPECT imaging have introduced the possibility to visualize radioactivity distribution using short frame times (13–17). Some cases where short frames have been applied are the evaluation of tubular filtration, renal clearance and kidney excretion (18–20). Furthermore short frames have been utilized in

hepatobiliary and cardiac scans (16). Moreover, fast dynamic ^{131}I SPECT has been utilized in the case of thyroid function studies which can be highly valuable for development and optimization of targeted cancer therapies (17).

On the other hand, the capability for short frames is accompanied by limited collected information due to the small number of photons captured by the system detectors in these short time intervals. This problem is enhanced in the case of conventional (non-stationary) SPECT imaging systems. This type of SPECT systems employs mechanically rotating detectors (or collimators) to scan an object (or an animal). The need of rotating the detector heads in order to increase angular sampling poses a challenge for fast dynamic imaging. The dead time (i.e., the time interval during which the detector is moving between two consecutive acquisition positions/projections) contributes in the increase of the scan times while it causes temporal resolution deterioration. During these time intervals the system is unable to detect any photons emitted by the injected tracer resulting in low sensitivity scans with poor temporal and spatial resolution.

This challenge has been partially mitigated by equipping the detector head(s) of those systems with multi-pinhole collimators. These apertures offer an increase in the angular sampling since they provide data acquisition from multiple angles simultaneously. Furthermore, stationary SPECT systems (no detector or collimator motion) also equipped with multi-pinhole collimators have been introduced to deal with the challenge of dead time (21–24).

The objective of this study is to investigate and compare the performance of two preclinical SPECT systems (NanoScan, VECTor), to perform short time frame imaging (ranging from few seconds up to 10 minutes duration). Towards this end, phantom experiments have been conducted to evaluate the systems performances for these short time intervals. In addition, the performance of the fast imaging modes provided by NanoScan was investigated prior to the systems comparison. The fast imaging modes feature a small number of detector angular positions per scan (1,2 and 3). The optimal performing fast imaging mode of NanoScan was selected for the systems comparison experiment. The performance evaluation study has been performed with respect to absolute quantification, noise levels and visual assessment of the acquired images.

Chapter 2

Materials & Methods

2-1 The imaging systems

2-1-1 NanoScan

NanoScan is a hybrid preclinical SPECT/MR imaging system from Mediso (Mediso,Ltd., Budapest, Hungary) (see figure 2-1a). The SPECT component of the system is based on a four-head rotating SPECT camera. Each of the 4 heads includes a 9.5 mm thick thallium-doped sodium iodide crystal.

NanoScan was equipped with a new high-sensitivity sixteen-pinhole aperture set of collimators developed and provided by the manufacturer (HS-APT62). This collimator setup includes pinholes with different diameters and overlapping projections on the detectors surface (figure 2-1b). The Field of View (FOV) of NanoScan for a single-bed position (Central Field of View, CFOV) when equipped with the APT62 is 30x30x11mm.

The MR component of the imaging platform is coupled in line with its SPECT component. The 1-T vertical field, horizontal-bore permanent magnet has maximal 5-ppm homogeneity throughout the FOV. The gradient subsystem can deliver 450 mT/m pulses. Two radiofrequency volume coils are available: a 35-mm- and a 60-mm-diameter coil recommended for mouse and rat imaging, respectively. In the present study the 35mm diameter coil was utilized. However, in one of the experiments there was a need to use the 60mm diameter coil due to size limitations (see section 2-4-2).

Besides conventional (helical) acquisition mode, the NanoScan system provides three acquisition modes suitable for fast imaging: a stationary acquisition mode without detector motion and two semi-stationary modes. In the first semi-stationary mode (Semi-2), SPECT data are acquired in two detector positions (projections) displaced by 45 degrees. In the second semi-stationary mode the data are acquired in three different positions (Semi-3). In that mode the second and third detector positions are displaced by 30 and 60 degrees respectively from the initial acquisition position. No translation of the mouse bed is performed when using the stationary and semi-stationary imaging modes. A summary of the fast acquisition modes of NanoScan is given in table 2-1.

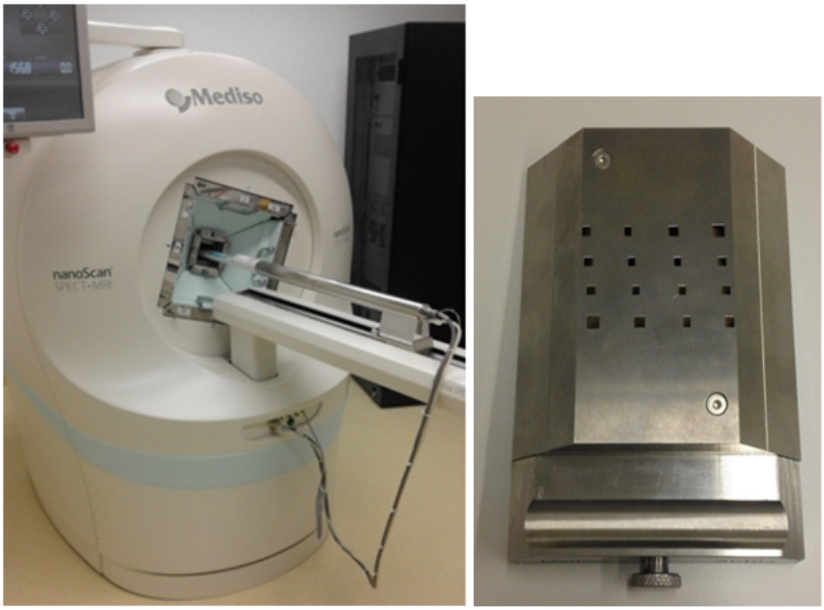

(a) **(b)**

Figure 2-1: (a) The preclinical SPECT/MR system in AMIEf, Erasmus MC, Rotterdam, (b)One of the four high-sensitivity collimators of the SPECT/MR system

Imaging Mode	Detector Positions / Projections	Projection Angles (in degrees)
Stationary	1	0
Semi-2	2	0, 45
Semi-3	3	0, 30, 60

Table 2-1: The fast imaging modes of NanoScan

2-1-2 VECTor

The second preclinical system utilized in the imaging studies was the VECTor from MILabs (MILabs B.V., Utrecht, Netherlands) (see figure 2-2a). Its SPECT subsystem is composed of three NaI(Tl) gamma detectors positioned in a triangular setup. Each detector crystal has a surface of 472x595mm and a thickness of 9.5mm.

The VECTor was equipped with an Ultra High Sensitivity Mouse imaging collimator (XUHS-M) (see figure 2-2b). The collimator is cylindrical and has 54 pinholes drilled in it. The diameter of each pinhole is 2.0mm. All pinholes together form an hourglass-shaped FOV. The central part of the FOV (CFOV) is an ellipsoid of 12x12x7mm and provides complete data without any bed movement. This design allows the count yield from a target organ to be increased (25) but also allows imaging of larger regions up to (dynamic) whole-body mouse scans (14, 23) by translating the animal bed into 3 dimensions using an XYZ stage. For most cases, this translation can be done quickly enough to still enable a combination of multiple-position acquisitions and dynamic imaging at a time scale of tens of seconds up to a few minutes. The data are collected in list-mode. A more detailed description of the system (3) and the collimator design (16) has been previously published.

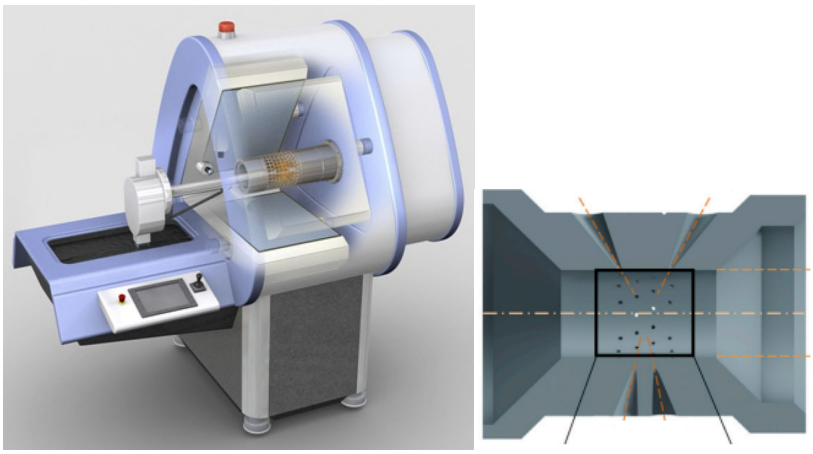

(a) (b)

Figure 2-2: a)The VECtor imaging system (3), (b) Cross-section of the Extra Ultra High Sensitivity collimator equipped to the VECTor (16)

The CT component of the system is composed by an x-ray source and an x-ray detector. The source is a sealed air-cooled X-ray tube operating between 20 and 65kV.The detector is a 1280x1024x82 bit digital X-ray camera with typical exposure of 120ms (minimum exposure 40ms). The total scanning area of the CT component has a 82mm diameter and 210mm length.

2-1-3 Systems Calibration

The SPECT subsystem of NanoScan was calibrated prior to experiments according to the manufacturer's instructions. The calibration was performed by using a 5ml-syringe filled with approximately 50MBq (Tc-99m). The activity in the syringe was measured with a dose calibrator before the SPECT scan. A Volume of Interest (VOI) was drawn in the reconstructed image enveloping the whole activity. The activity measured in the VOI was corrected for radioactive decay. Afterwards, the calibration factor was calculated based on the formula:

$$f = \frac{A_{calib}}{A_{VOI}} \tag{2-1}$$

where A_{calib} is the activity of the syringe measured in the dose calibrator and A_{voi} is the radioactive decay corrected amount of activity measured within the VOI. The VECTor had been already calibrated before conducting the experiments.

2-2 Phantoms & Image Quality Parameters

Three different types of phantoms were utilized in the imaging studies in order to evaluate the imaging performance of the systems. Each type of phantom was used to assess different parameters of image quality. Firstly, the quantification accuracy with NanoScan in uniform

phantom (syringe) was investigated. Afterwards, an experiment was executed with the NU4IQ phantom in order to select the best performing fast imaging mode of NanoScan in terms of angular sampling. Finally, the systems comparison study was conducted with the SPECTIQ phantom. The reconstructed images of this study were analyzed in MATLAB (MATLAB and Statistics Toolbox Release 2016b, The MathWorks, Inc., Natick, Massachusetts, United States).

2-2-1 Syringes

The simplest structure phantoms used in this study were cylindrical homogeneity phantoms (syringes) with 10ml volume and an inner diameter of 14.5mm. Syringes have been used in quantification accuracy experiments in order to assess the activity recovery in the reconstructed images (15, 26).

In the current study, the total activity in the reconstructed syringes images was measured by drawing a large Volume Of Interest (VOI) enveloping the whole phantom volume within the FOV and summing all the activity within that volume (2, 15). The activity measured in the VOI was corrected for radioactive decay and afterwards was compared with the true total activity measured with the dose calibrator.

The activity recovery coefficient (RC) (26) was employed in order to characterize the modes performance for accurate quantification. RC is defined as the measured apparent radioactivity concentration divided by the true activity concentration:

$$RC = \frac{A_{VOI,corr}}{A_{orig}} \tag{2-2}$$

Since the dose calibrator measures only the total activity in a phantom, the activity concentration in each phantom was calculated by measuring the mass of the radioactive solution in the phantom. The mass of the radioactive solution was measured by weighing the phantom before (empty) and after (full) addition of the radioactive solution. The same approach was applied to the other phantom used in this study in order to measure the activity concentration inside them.

In addition to the quantification study, the dataset was analyzed in order to measure the noise levels in the reconstructed images. Homogeneity phantoms (syringes) or uniform regions of more complicated structure phantoms have been utilized in several studies in order to assess noise levels in the reconstructed images (15, 27–30) . Regions Of Interest (ROIs) were drawn on each of the 10 central slices of the reconstructed volume. The diameter of each ROI was equal to 75% of the active phantom diameter in order to avoid partial volume effects (Figure 2-3). The noise levels were determined by measuring the relative standard deviation (also known as coefficient of variance) of the voxel intensities in these ROIs:

$$\%STD = CV\% = \frac{\sigma}{\mu} \times 100 \tag{2-3}$$

where σ and μ are the standard deviation and the mean intensity value of the voxels in the ROI.

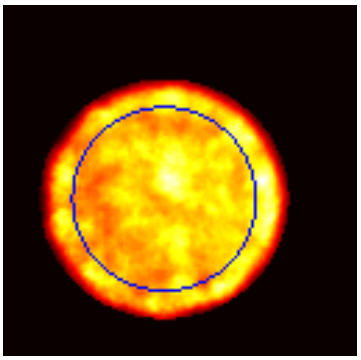

Figure 2-3: The blue circle indicates the ROI applied on each slice in order to measure noise levels in the reconstructed images of syringes

2-2-2 NU4IQ phantom

The NEMA NU 4 image quality phantom (NU4IQ)(figure 2-4) was used in order to compare the ability of each fast imaging mode of NanoScan to recover activity from small diameter structures. Despite the fact this phantom has been designed and implemented for the characterization of the imaging performance of preclinical PET systems (31–33), it has been also utilized in preclinical SPECT studies (27). The NU4IQ phantom has a main fillable chamber (uniform region). The chamber has a 30mm diameter and 30mm length. The phantom has also a solid acrylic glass region with 5 fillable rods drilled through. Their diameters are 1, 2, 3, 4 and 5mm. Furthermore, it consists of a lid attached to the uniform region of the phantom. The lid includes two cylindrical cold region compartments. These structures are hollow and have an inner diameter of 8mm and a length of 15mm. The two compartments are filled with water and air respectively.

Figure 2-4: The NEMA NU 4 Image Quality (NU4IQ) phantom

The activity recovery in the rods was assessed by calculating the recovery coefficient. The measurements were performed based on the NEMA measuring approach (31). The image slices covering the central 10mm length of the rods was averaged to obtain a single image slice of lower noise. Circular ROIs were drawn in this image around each rod. The maximum intensity voxels were found in each ROI. The coordinates of those voxels were used to create line profiles in the axial direction. The mean of the voxel intensity values measured along each profile were divided by the activity concentration measured with the dose calibrator in order to calculate the recovery coefficients:

$$RC_{rod} = \frac{\mu_{lineprofile}}{\mu_{dosecalibrator}} \tag{2-4}$$

2-2-3 SPECTIQ phantom

Besides the NU4IQ phantom, a down-sized version of it (SPECTIQ phantom) (28), designed especially for preclinical SPECT systems performance characterization, was also utilized in the systems comparison study. The phantom structure is identical to the NU4IQ phantom structure (figure 2-5). The size of this phantom is approximately 70% the size of the original phantom. The rods diameters of the SPECTIQ phantom are 1.5, 1.0, 0.75, 0.5 and 0.35mm. The rods length is 6.5mm. The inner dimensions of the uniform region of this phantom are 21x21mm. Furthermore, the cold compartments have an inner diameter of 5.6mm and a length of 10.5mm.

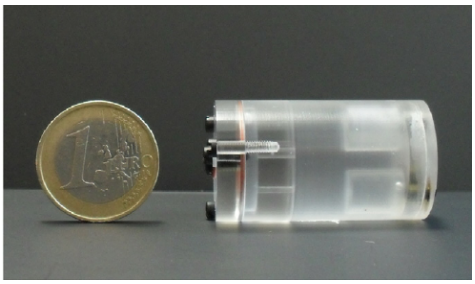

Figure 2-5: The SPECTIQ phantom: the down-sized version of the NU4IQ phantom (28)

The image quality parameters associated with the SPECTIQ phantom were extracted from the NEMA NU 4 guidelines (31) and they are adapted according to the smaller dimensions of the phantom as in the study of Visser et al (28)

Uniform Region

A 15.75mm diameter (75% of the active diameter) by 7mm length cylindrical VOI was drawn over the center of the uniform region of the phantom. The cylinder length corresponds to the central two-thirds of the active length. The average activity concentration along with the maximum, the minimum and the relative standard deviation in the VOI were measured. In addition to the NEMA guidelines, the recovery coefficient in the uniform region was measured by comparing the mean activity concentration in this phantom section with the measurement performed with the dose calibrator:

$$RC_{uniform} = \frac{\mu_{uniform}}{\mu_{dosecalibrator}} \tag{2-5}$$

Rods

The image slices covering the central half length of the rods (3.25mm) were averaged to obtain a single image slice of lower noise. Large circular ROIs were drawn in this image, around

each rod. The maximum values in each of these ROIs were measured. The transverse image pixel coordinates of the locations with the maximum ROI values were recorded and used to create line profiles along the rods in the axial direction. The pixel values measured along each profile, divided by the mean activity concentration measured in the uniform region (μ uniform), were used to determine the mean and standard deviation of the recovery coefficient for each rod size:

$$RC_{rod} = \frac{\mu_{lineprofile}}{\mu_{uniform}} \tag{2-6}$$

$$\%STD_{RC} = 100 \times \sqrt{(\frac{\sigma_{lineprofile}}{\mu_{lineprofile}})^2 + (\frac{\sigma_{uniform}}{\mu_{uniform}})^2} \tag{2-7}$$

Cold Compartments

Cylindrical VOIs were defined in the water- and air-filled cylindrical compartments. The diameter of the VOI was 2.8 mm (half the physical diameter of the cylinders) and encompasses the central 5.25 mm in length (Figure 2-6). The ratio of the mean in each cold region to the mean of the uniform area was reported as spill-over ratio (SOR).

$$SOR = \frac{\mu_{compartment}}{\mu_{uniform}} \tag{2-8}$$

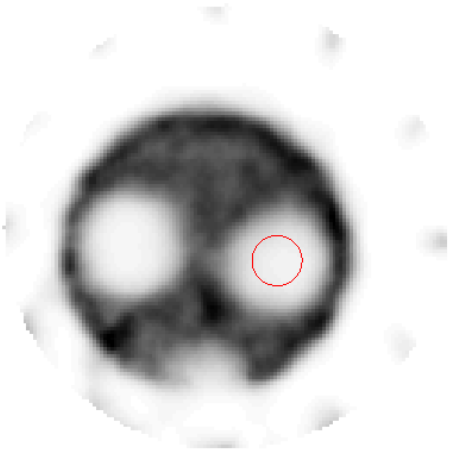

Figure 2-6: The ROI (in red) used for the measurement of SORs. Same size ROIs have been used for both cold compartments SOR

2-3 Radionuclide

All phantoms used in the study were filled with radioactive solutions of the isotope Tc-99m (half-life: 6 hours), which has been mainly used in performance characterization studies of preclinical imaging systems (29, 34, 35).

2-4 Image Acquisition

2-4-1 Quantification Accuracy Experiment

A 10ml syringe was filled with 274.97MBq (5ml solution) for determining and comparing the ability of the fast imaging modes of NanoScan to recover activity for different short frames (6, 12, 18, 24 and 30s). This approach yielded an experiment with consecutive image acquisitions of different frames. No translation of the mouse bed was performed during the experiment (single position). The frame times were selected in such a way that they could be divided perfectly in all three different cases of angular sampling (1,2 and 3 projections).

2-4-2 Fast Imaging Mode Selection Experiment

The NEMA NU 4 image quality phantom (NU4IQ) was filled with 120MBq (10.3MBq/ml) and scanned for different time frames (6, 12, 18, 24, 30s) for comparing the ability of each fast imaging mode of NanoScan to recover activity from small diameter structures. No translation of the mouse bed was performed during the experiment (single position). It should be mentioned due to the size limitations the 60mm rat imaging MR coil was used. In order to keep the signal of the MR image in the same levels as in the previous study, the number of pulse excitations was doubled (2 excitations).

2-4-3 Systems Comparison Experiment

For the last experiment, a comparison of the short frames imaging performance between the NanoScan and the VECTor was conducted. The SPECTIQ phantom (28) was filled with 2.95MBq/ml (20MBq). Acquisitions of different frame times were performed. Specifically, images with frame duration of 18, 36, 72, 180, 360 and 600s covering the whole radioactive volume of the phantom, were acquired (whole body scans).

The whole body scans were performed in different ways for the two systems. In NanoScan experiment, the scan was performed in three different axial bed positions (Figure 2-6). In each position a different section of the SPECTIQ phantom was scanned (rods, uniform region, cold compartments) utilizing the Semi-3 imaging mode. This imaging mode was selected based on the results of experiments 2-4-1 and 2-4-2. As a result, the whole phantom volume was covered with consecutive and non-overlapping FOVs, creating a larger FOV with axial length of 33mm (Figure 2-6). The scan was executed in this manner due to the limited size of the axial FOV provided by the collimator aperture used (FOVz = 11mm) compared to the active length of the phantom (29.95mm).

On the contrary the XYZ stage of VECTor allowed the adjustment of the FOV based on the phantom geometrical dimensions. In order to keep the FOVs between the two systems as equal as possible, a 33mm length axial FOV was selected. A spiral mode and 100 frames dynamic acquisition with 6s per frame covering the whole phantom body was performed with VECTor. The images were reconstructed based on the list-mode of the system. By employing the 6s whole body acquisition frames, the desirable frame times were acquired. In figure 2-7, the diagram summarizes the imaging study execution for a specific whole body frame time (360s).

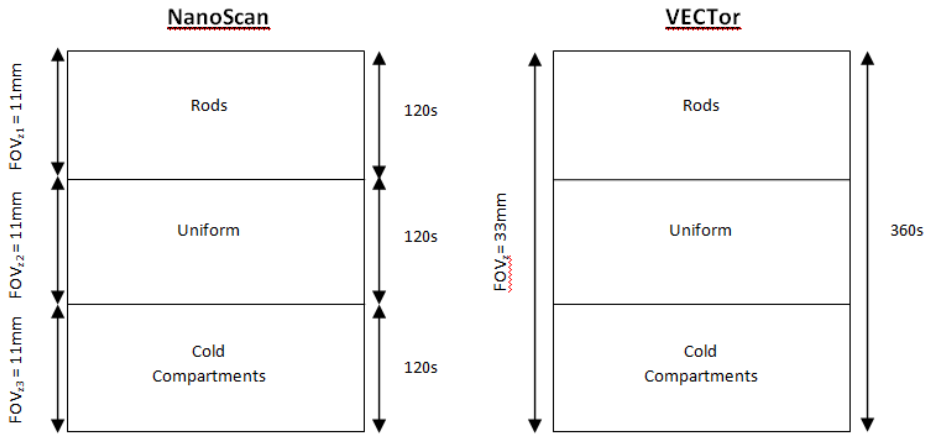

Figure 2-7: Diagram of the imaging study execution for a specific whole body frame time (360s). The two large rectangles represent the SPECTIQ phantom volume and is divided in the three phantom sections. The acquisitions with NanoScan were divided in three steps resulting in three consecutive and non-overlapping FOVs

This SPECTIQ phantom was selected in this experiment due to impracticality purposes. Because of its large size, the NU4IQ phantom couldn't fit in the mouse bed of the VECTor. Furthermore, the mouse bed couldn't be replaced by the rat bed of the same system, because such a modification would demand the replacement of the mouse imaging collimator with the rat imaging collimator.

2-5 Image Reconstruction

The image reconstruction in NanoScan was performed using a Maximum Likelihood Expectation Maximization (MLEM) algorithm (36). The default reconstruction settings provided by the system reconstruction software (Nucline) were used (1 subset and 48 iterations). Attenuation correction was applied using a material map. The acquisition parameters of the material map were: 30-degree flip angle, T_R=4.3ms, T_E=1.4ms, 1 excitation and 2mm slice thickness. The material map was segmented in air and water to obtain the attenuation correction map. Scatter correction was also applied. The reconstruction resulted in images matrices of 128x128x43 and voxel sizes of 0.258mm in all dimensions. A 20% wide phototpeak window was automatically applied.

For VECTor, the images were reconstructed based on the list-mode of the system. By employing the acquisition frames, the desirable frame times were acquired. A pixel-based ordered subset expectation maximization (POSEM) algorithm (37) with 4 subsets and 30 iterations was utilized. This specific combination of iterations and subsets was applied based on regular users' recommendations. The voxels dimensions (0.168mm in all directions) were set as equal as possible to the ones of NanoScan images. A 20% wide photopeak window was applied. Attenuation correction was performed through the CT data. Scatter correction was performed through triple energy windows method. A post reconstruction Gaussian filter with FWHM of 1mm was applied to the images.

Chapter 3

Results

3-1 Quantification Accuracy Experiment

Strong spatial distortion at the edges of the syringe volume are observed when using the stationary mode of NanoScan (Figure 3-1a). The reconstructed volume appears to have square shape (Figure 3-1a) The image spatial distortion is reduced as the number of projections increases (Figure 3-1b,c). The shape of the syringe in the image appears to be more round when using the semi-stationary modes of NanoScan (Figure 3-1b,c). The increase of angular sampling appears to provide images with better uniformity (Figure 3-2). The images in Figures 3-1 and 3-2 are representative data of the study. For data completeness the reader is referred to Appendix A.

The activity recovery remained almost stable for all frame times and number of projections used(Figure 3-3a). A highest of 5% deviation from the dose calibrator measurement was found in the 12s frame when using the stationary mode. The increase of the time frames resulted in images with lower noise levels (Figure 3-3b). Images acquired with the Semi-3 imaging mode had lower noise levels (Figure 3-3b).

3-2 Fast Imaging Mode Selection

Strong spatial distortion artifacts were observed when using the stationary imaging mode of NanoScan (Figure 3-4a,d,g). The image artifacts become less pronounced when using the semi-stationary modes of NanoScan (Figure 3-4,b,c,e,f,h,i). Furthermore, activity "spillover" and noise artifacts are observed in the image background when using the stationary mode. The artifacts become less pronounced when the angular sampling and the frame time is increased. The images in Figure 3-4 are representative data of the study. For data completeness the reader is referred to Appendix B.

There is a significant activity overestimation for all frame times and imaging modes used in the study (Figure 3-5). This overestimation is enhanced especially in the case of the 4- and

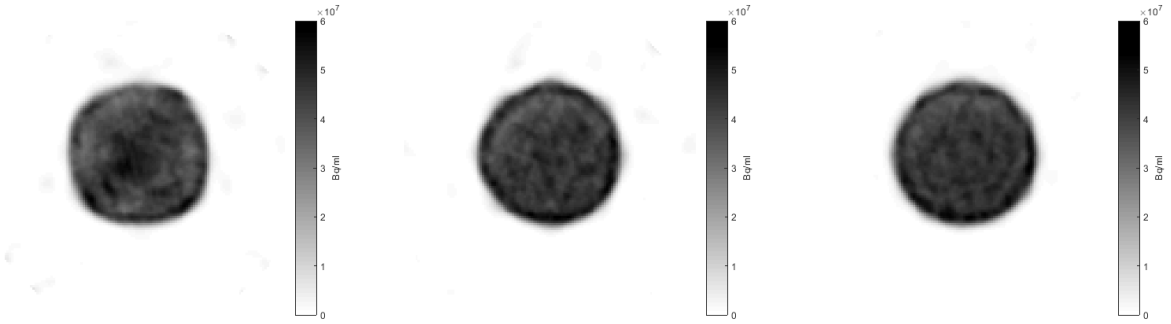

(a) Stationary **(b)** Semi-2 **(c)** Semi-3

Figure 3-1: Reconstructed transaxial slices of a 10ml syringe acquired with 30s frame times and with the fast imaging modes of NanoScan. Spatial distortion artifacts become less pronounced as the angular sampling increases.

3-mm diameter rods of the NU4IQ phantom. The overestimation is smaller in the case of the 5mm diameter rod. In the case of the 5-mm diameter rod the dose calibrator measurement lies within the variation interval of the activity recovery for all imaging modes and frame times used. The Semi-3 mode appears to provide more accurate activity recovery in the 2mm diameter rod. The dose calibrator measurement lies within the variation interval of the activity recovery when using Semi-3 for all frame times (Figure 3-5). However, the difference is significant only in the case of the 30s frame (Figure 3-5a). Finally, none of the modes could fully recover the smallest phantom rod (d=1mm) for all different frames used in this experiment.

3-3 Systems Comparison Experiment

Uniform Region

Images acquired with NanoScan appear to have better uniformity (Figures 3-6,3-7). The images in Figures 3-6 and 3-7 are representative data of the study. For the complete dataset the reader is referred to Appendix C. Both systems provided accurate activity recovery in the uniform region of the SPECTIQ phantom (active diameter: 21mm) with up to 5% deviation from the dose calibrator measurement in the case of the 18s frame(Figure 3-8a,b). The noise levels (%STD) in the reconstructed images of both systems are reduced as the frame time increases (Figure 3-8c,d). NanoScan provided images with lower noise levels than VECTor (Figure 3-8c,d). Furthermore, the noise levels (%STD) in the images acquired with NanoScan appear to reach convergence after the 180s frame (Figure 3-8d).

Rods

Both systems could recover the three largest rods (d= 1.5, 1.0, 0.75mm) of the phantom for the two longest frames used (600s, 360s). On the contrary, none of the systems could recover two smallest phantom rods (d=0.5mm, 0.25mm). As the frame times decrease, artifacts are observed in the images acquired with VECTor (Figure 3-9). The 1.0mm-diameter rod couldn't

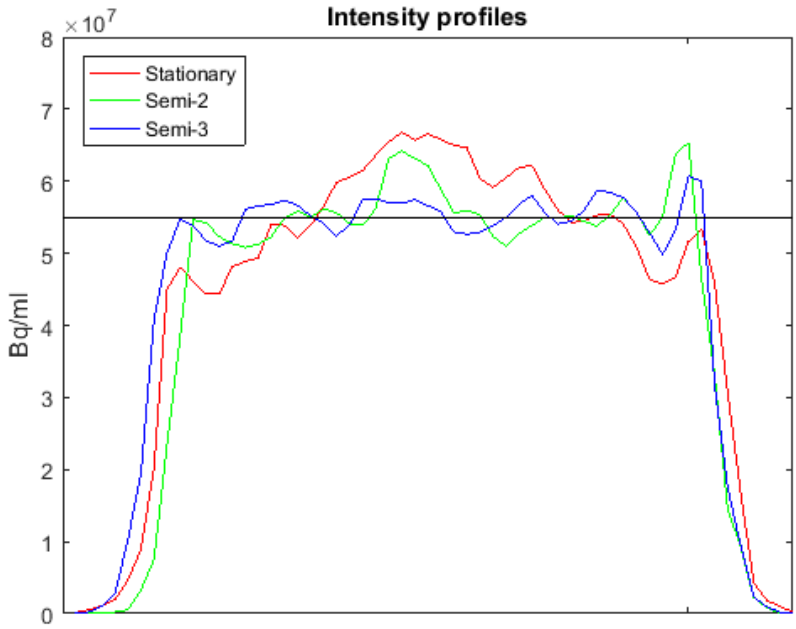

Figure 3-2: Intensity profiles drawn through the reconstructed syringe volume. Each profile corresponds to a different fast imaging mode. The increase of angular sampling appears to provide images with better uniformity

be recovered with NanoScan when imaging with the shortest time frames used (18, 36, 72s) (Figure 3-10b). The same rod couldn't be recovered when imaging with the VECTor for the two shortest frames (18, 36s) (Figure 3-10c). Furthermore, in the shortest frame (18s), only the largest rod (d=1.5mm) appears in the images acquired with NanoScan. The images in Figure 3-9 are representative data of the study. For the complete dataset the reader is referred to Appendix C.

There is overestimation in the activity recovery in the 1.5mm-diameter rod in the images acquired with VECTor (Figure 3-10a). However the ground truth value lies within the variance interval. Images acquired with NanoScan provided less activity recovery in the same rod (Figure 3-10a). As the frame time decreases activity overestimation appears to increase for both systems while the difference in activity recovery doesn't appear to be significant (Figure 3-10a).

VECTor provided higher activity recovery than NanoScan in the 1mm diameter rod of the phantom when imaging with the 600-,360- and 180s frames (Figure 3-10b). VECTor appears to provide better quantification for the 72- and 36s frames (Figure 3-10b). For the shortest frame used (18s) the VECtor provided overestimated activity recovery, while NanoScan couldn't recover the rod at all (Figure 3-10b).

There is no clear distinction about the performance of the systems when imaging the 0.75mm diameter rod (Figure 3-10c). NanoScan couldn't recover the rods when using the shortest frames (72,36,18s). VECTor couldn't recover that rod only in the case of the shortest frame (18s).

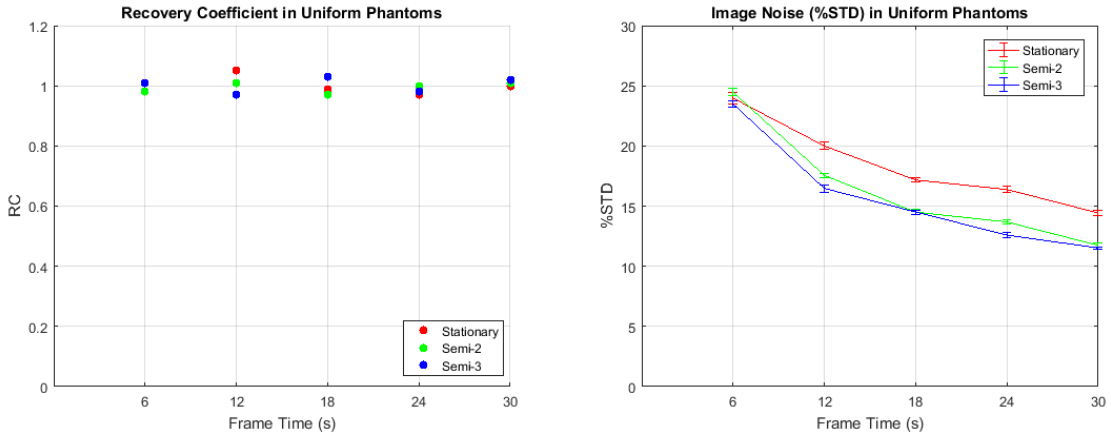

Figure 3-3: (a) Quantification accuracy in 10ml syringe as function of acquisition times using the fast imaging modes of NanoScan. The activity recovery remained almost stable for all frame times and number of projections used. A highest of 5% deviation from the dose calibrator measurement was found in the 12s frame when using the stationary mode. (b) Noise levels measured in the reconstructed images as a function of frame time. The increase of the time frames resulted in images with lower noise levels. Images acquired with the Semi-3 imaging mode have lower noise levels.

Spillover Ratios (SORs)

Reconstructed slices of the cold compartments section of the phantom and the corresponding line profiles show that SORs appear to be lower in the image acquired with VECTor (Figures 3-11,3-12). The images in Figures 3-11,3-12 are representative data of the study. For the complete dataset the reader is referred to Appendix C.

The increase of the frame time tends to provide images where the spillover effect is reduced (Figure 3-13). After a steep decline of the SORs when moving from the 18s to the 36s frame, the SORs appear to reach convergence (Figure 3-13). The spillover ratio in the water compartment is approximately 46.6% lower in VECTor than in NanoScan (after reaching convergence). In addition, the spillover ratio in the air-filled compartment is also lower in VECTor (approximately 22.2% after reaching convergence).

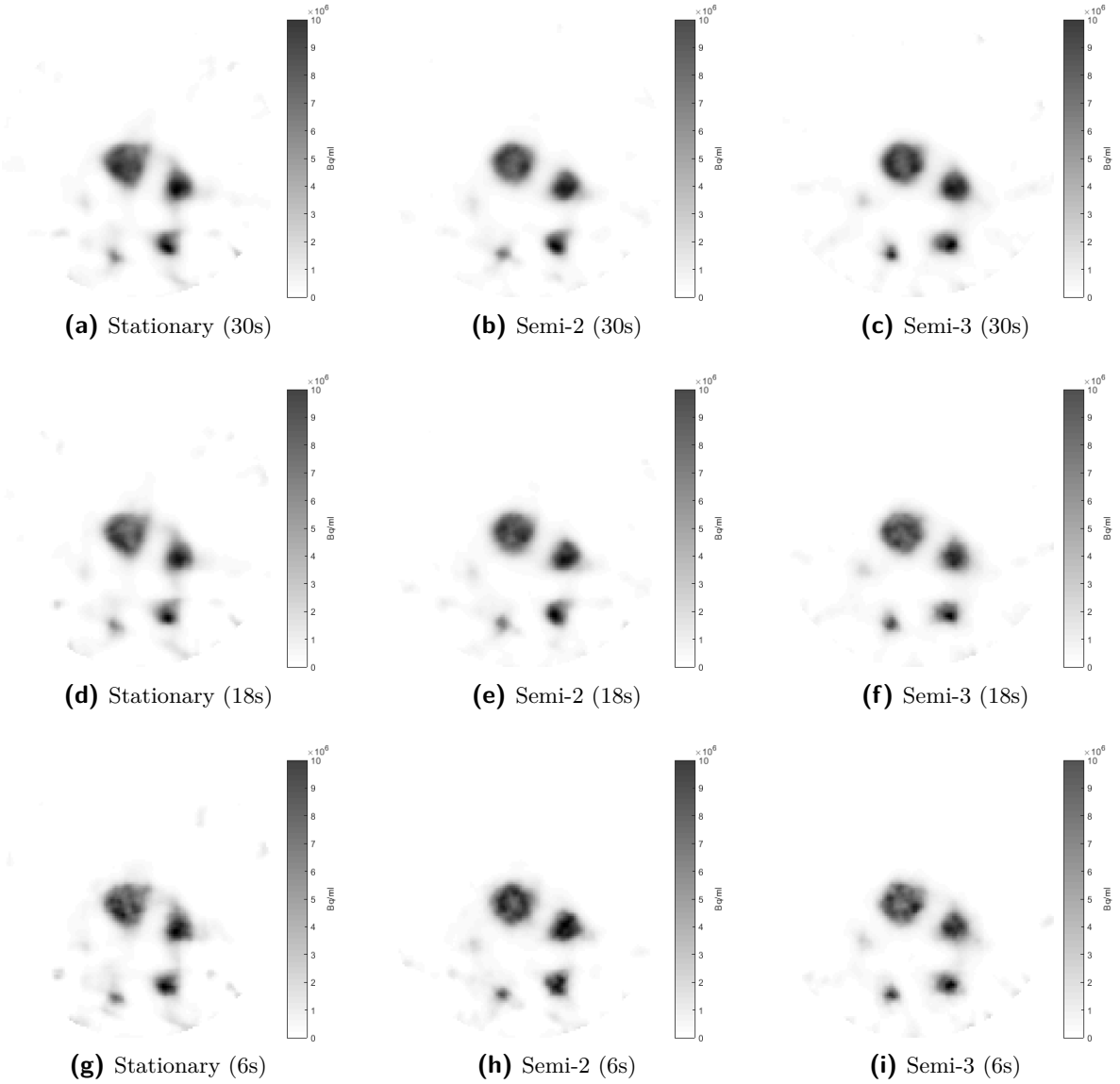

(a) Stationary (30s) **(b)** Semi-2 (30s) **(c)** Semi-3 (30s)

(d) Stationary (18s) **(e)** Semi-2 (18s) **(f)** Semi-3 (18s)

(g) Stationary (6s) **(h)** Semi-2 (6s) **(i)** Semi-3 (6s)

Figure 3-4: Reconstructed transaxial slices of the rod section of the NU4IQ phantom acquired with 30, 18 and 6s frames using all three fast acquisition modes. Starting from the top rod and moving clockwise, the rods diameters are: 5,4,3,2 and 1mm. Image artifacts become less pronounced as the frame time and the angular sampling increase.

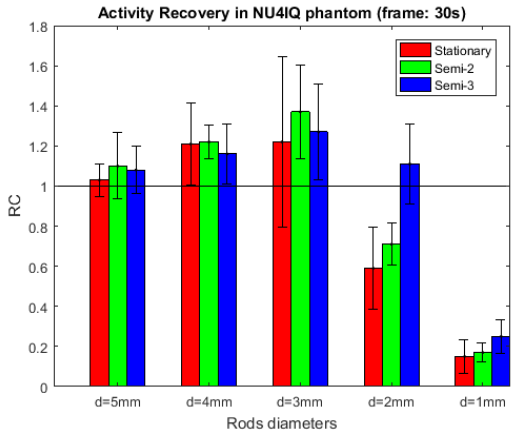

(a) 30s

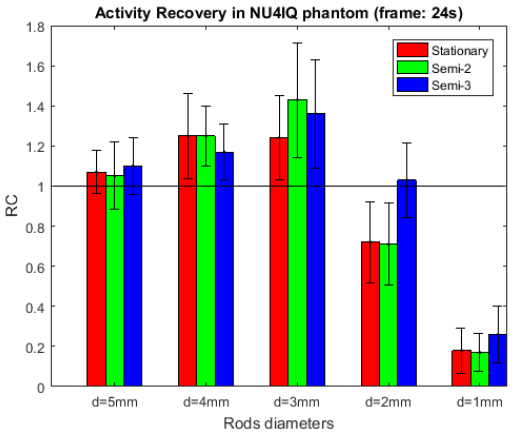

(b) 24s

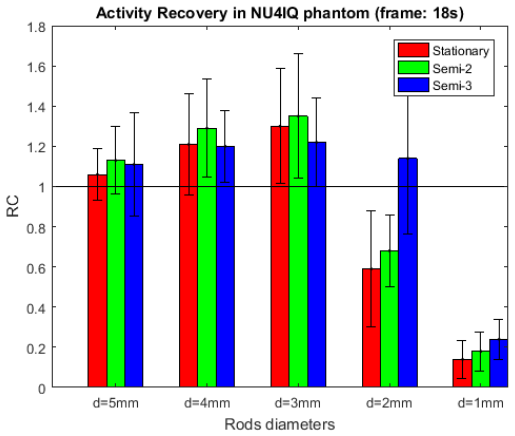

(c) 18s

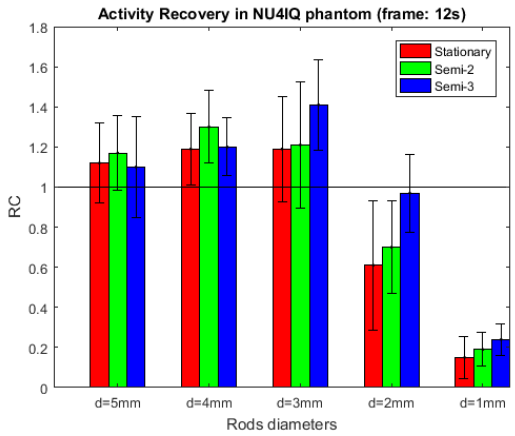

(d) 12s

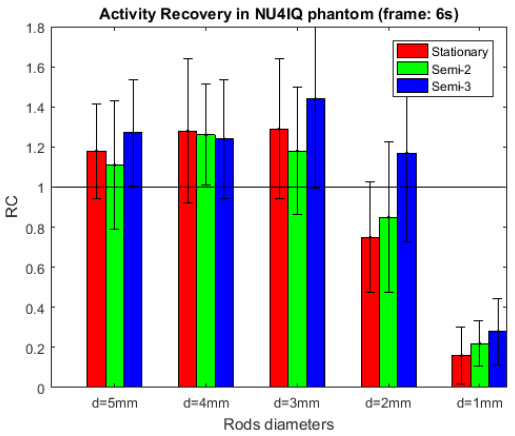

(e) 6s

Figure 3-5: Activity Recovery in the rods of SPECTIQ phantom for different frames (6,12,18,24,30s) and acquisition modes. There is a significant activity overestimation for all frame times and imaging modes used in the study (especially in the case of the 4- and 3-mm diameter rods). The Semi-3 mode provides significantly more accurate activity recovery in the 2mm diameter rod. None of the modes could fully recover the smallest phantom rod (d=1mm).

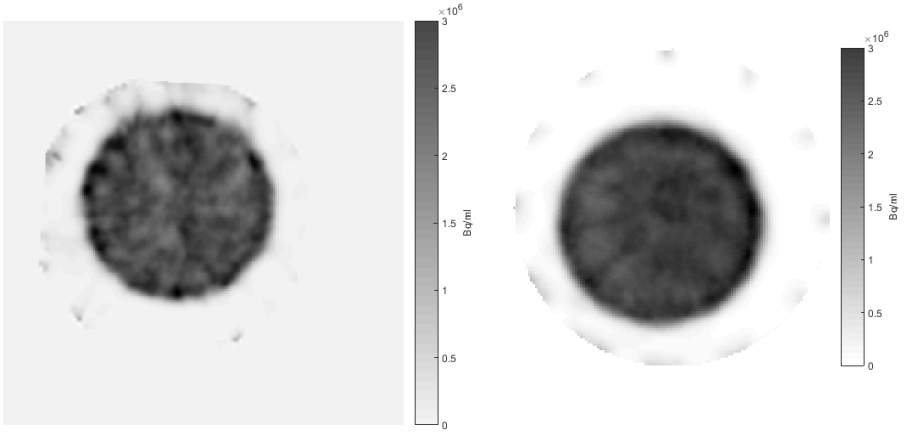

(a) VECTor (frame: 600s) **(b)** NanoScan (frame: 600s)

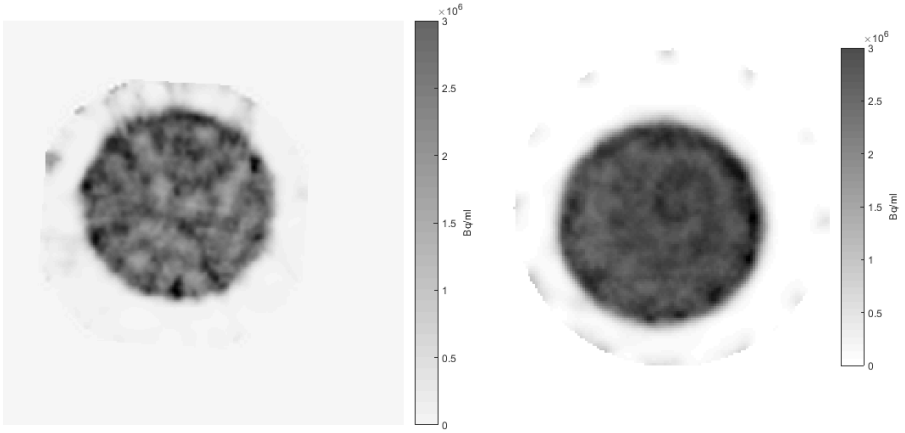

(c) VECTor (frame: 180s) **(d)** NanoScan (frame: 180s)

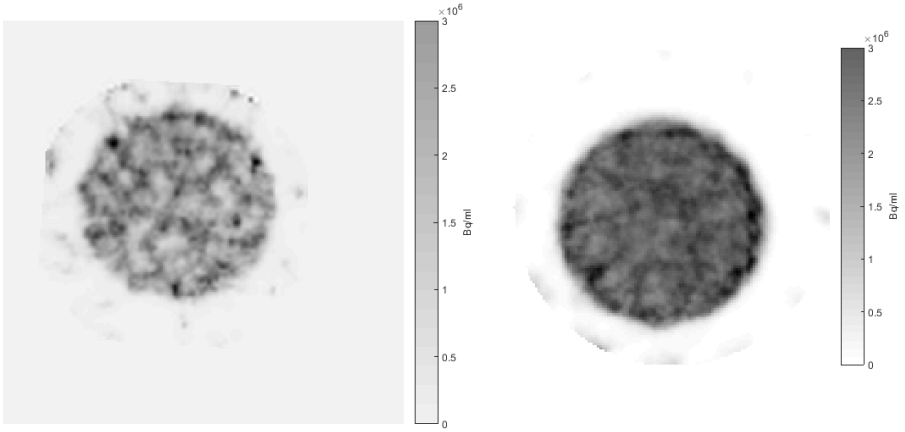

(e) VECTor (frame: 36s) **(f)** NanoScan (frame: 36s)

Figure 3-6: Reconstructed transaxial slices of the uniform region of the SPECTIQ phantom for 600,180 and 36s. Reconstructed images of the 360,72 and 18s frames can be found in Appenix C. NanoScan appears to provide images with better uniformity

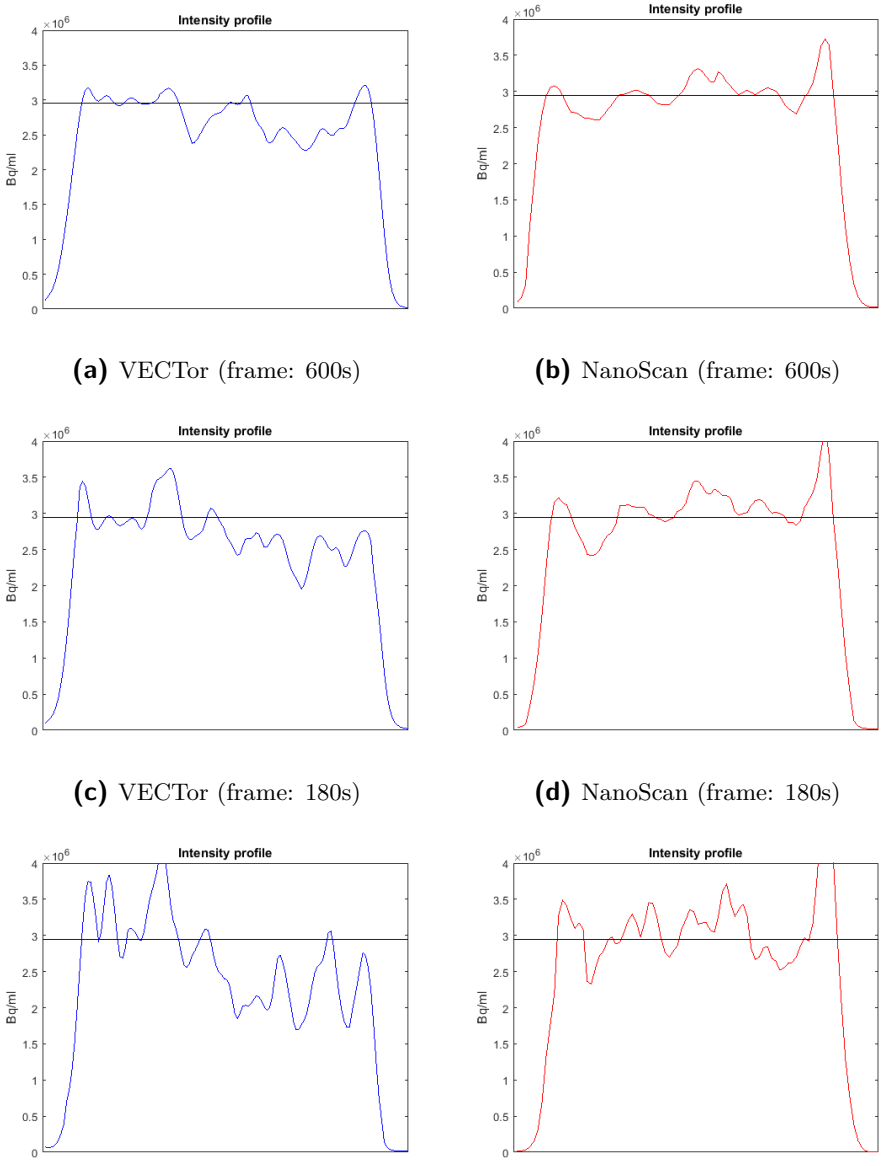

(a) VECTor (frame: 600s)

(b) NanoScan (frame: 600s)

(c) VECTor (frame: 180s)

(d) NanoScan (frame: 180s)

(e) VECTor (frame: 36s)

(f) NanoScan (frame: 36s)

Figure 3-7: Intensity profiles drawn through the reconstructed volume of the uniform region of the SPECTIQ phantom for 600,180 and 36s. Intensity profiles of the 360,72 and 18s frames can be found in Appendix C. NanoScan appears to provide images with better uniformity

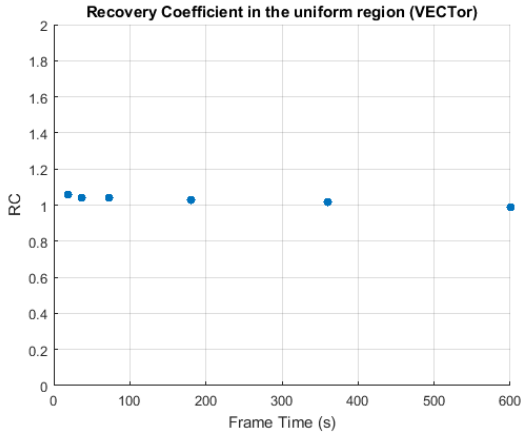

(a) Activity recovery in the uniform region of SPECTIQ phantom (VECTor)

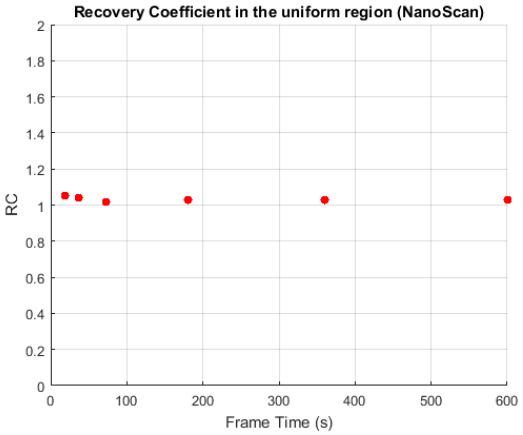

(b) Activity recovery in the uniform region of SPECTIQ phantom (NanoScan)

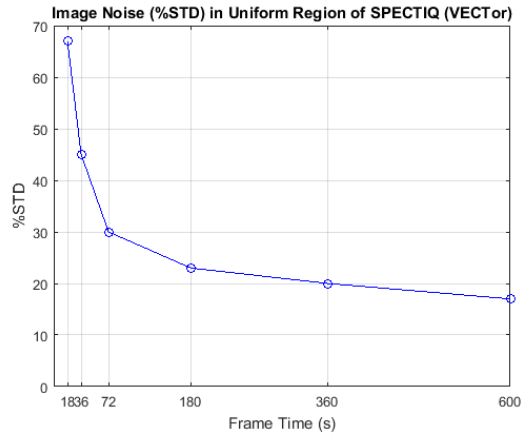

(c) Noise (%STD) in the uniform region of SPECTIQ phantom (VECTor)

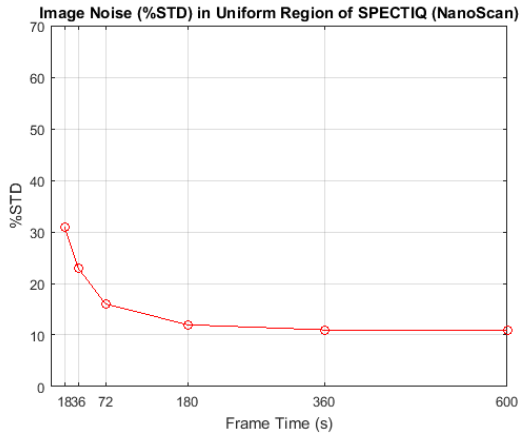

(d) Noise (%STD) in the uniform region of SPECTIQ phantom (NanoScan)

Figure 3-8: (a),(b) Activity recovery in the uniform region of both systems as a function of frame time. Both systems provided accurate activity recovery in this phantom section (active diameter: 21mm) with up to 5% deviation from the dose calibrator measurement. (c),(d) Noise (%STD) in the uniform region of the SPECTIQ phantom for both systems as a function of frame times. The noise levels in the reconstructed images of both systems are reduced as the frame time increases. NanoScan provided images with lower noise levels than VECTor. The noise levels in the images acquired with NanoScan appear to reach convergence after the 180s frame.

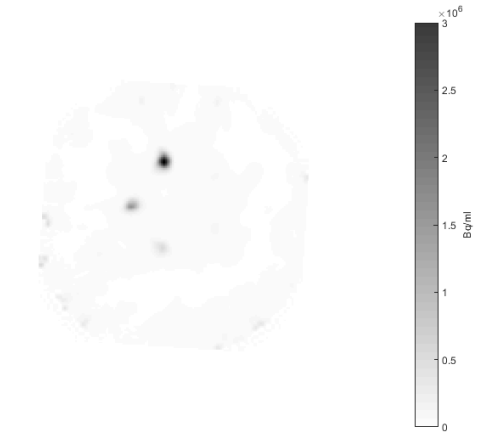

(a) VECTor (frame: 600s)

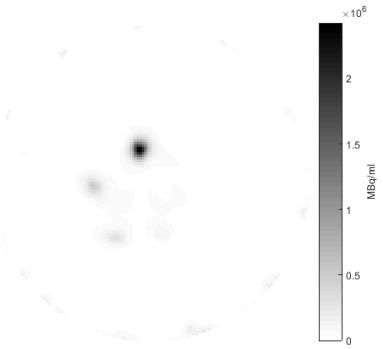

(b) NanoScan (frame: 600s)

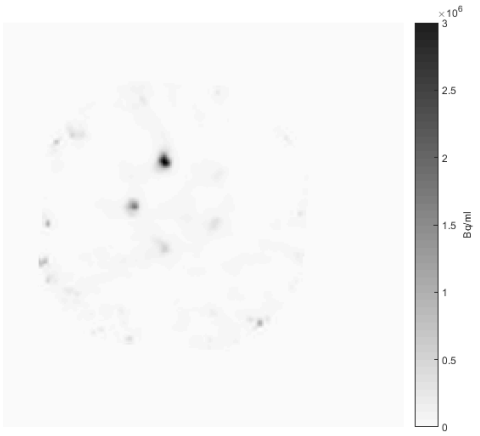

(c) VECTor (frame: 180s)

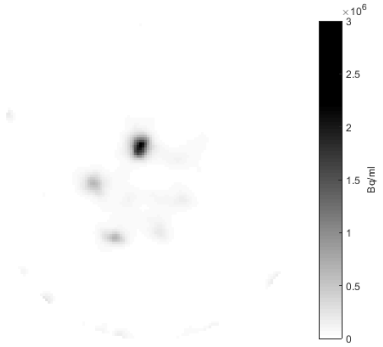

(d) NanoScan (frame: 180s)

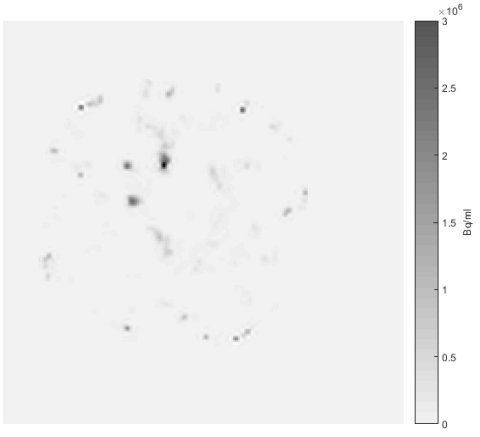

(e) VECtor (frame: 36s)

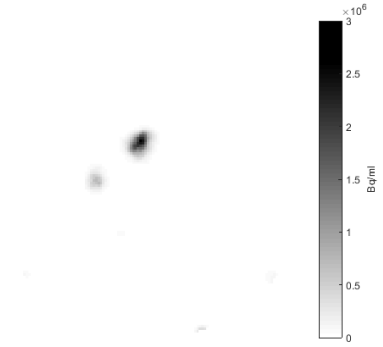

(f) NanoScan (frame: 36s)

Figure 3-9: Reconstructed transaxial slices of the rod section of the SPECTIQ phantom acquired with 600, 180 and 36s frames acquired with both systems. Starting from the top rod and moving counter-clockwise, the rods diameters are: 1.5mm, 1.0mm, 0.75mm. The 0.5mm and 0.35mm diameter couldn't be recovered.

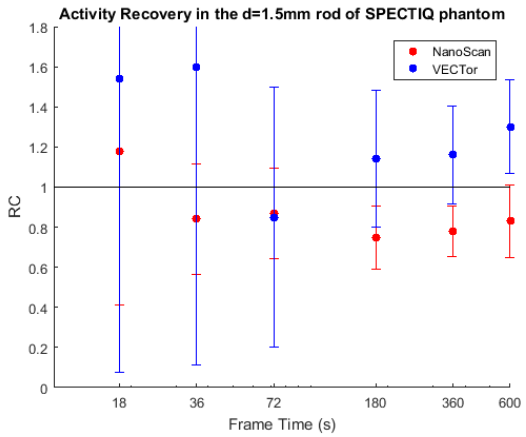

(a) Activity recovery in the 1.5mm diameter rod

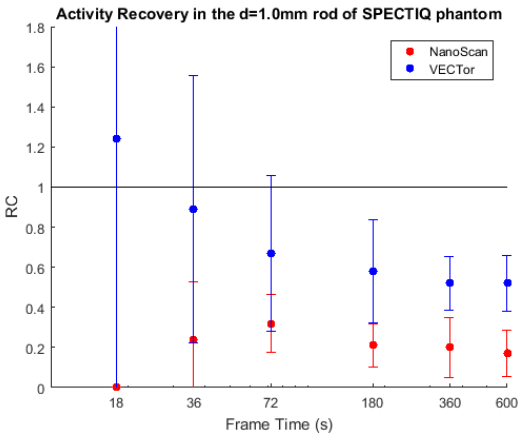

(b) Activity recovery in the 1mm diameter rod

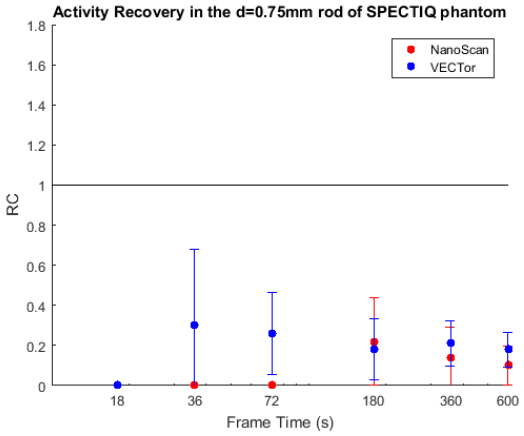

(c) Activity recovery in the 0.75mm diameter rod

Figure 3-10: Activity recovery of both NanoScan (red) and VECtor (blue) in three largest rods of SPECTIQ (d=1.5,1.0,0.75mm). The two smallest rods (d=0.5,0.35) couldn't be recovered. VECTor provided higher activity recovery than NanoScan in the d=1.5mm rod for the 600- and 360s frames. As the frame time decreases activity overestimation appears to increase for both systems while the difference in activity recovery doesn't appear to be significant. VECTor provided higher activity recovery than NanoScan in the 1mm diameter rod of the phantom when imaging with the 600-,360- and 180s frames. VECTor appears to provide better quantification for the 72- and 36s frames. For the shortest frame used (18s) the VECtor provided overestimated activity recovery, while NanoScan couldn't recover the rod at all

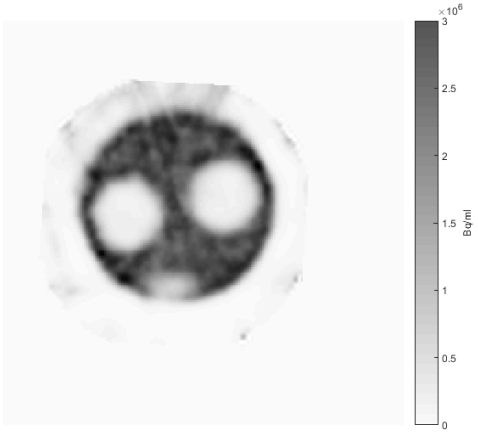

(a) VECTor (frame: 600s)

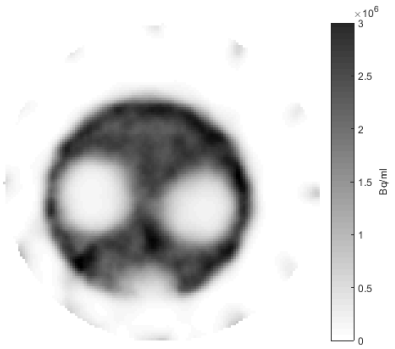

(b) NanoScan (frame: 600s)

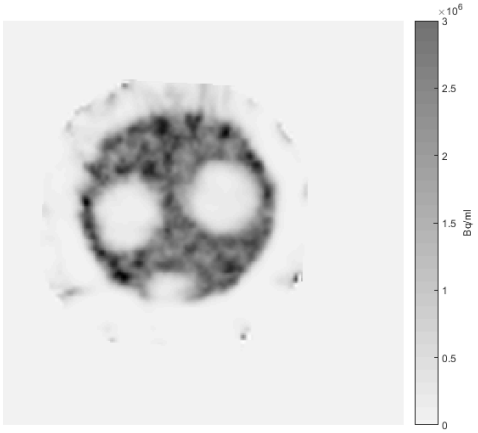

(c) VECTor (frame: 180s)

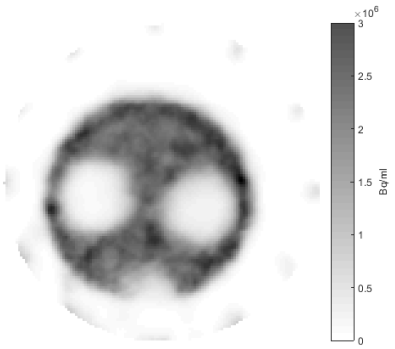

(d) NanoScan (frame: 180s)

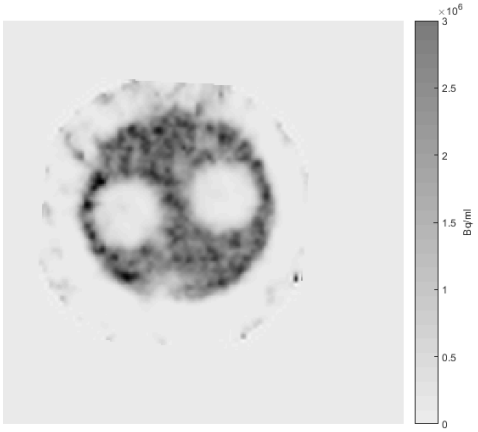

(e) VECTor (frame: 36s)

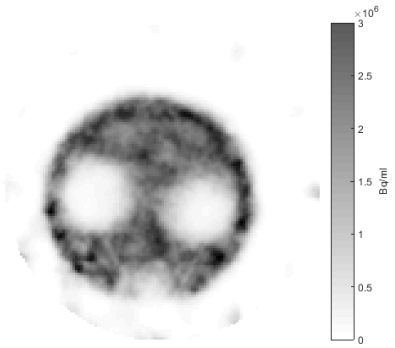

(f) NanoScan (frame:36s)

Figure 3-11: Reconstructed transaxial slices of the cold compartments section of the SPECTIQ phantom acquired with VECTor (a,c,e) and NanoScan (b,d,f). SORs appear to be lower in the image acquired with VECTor.

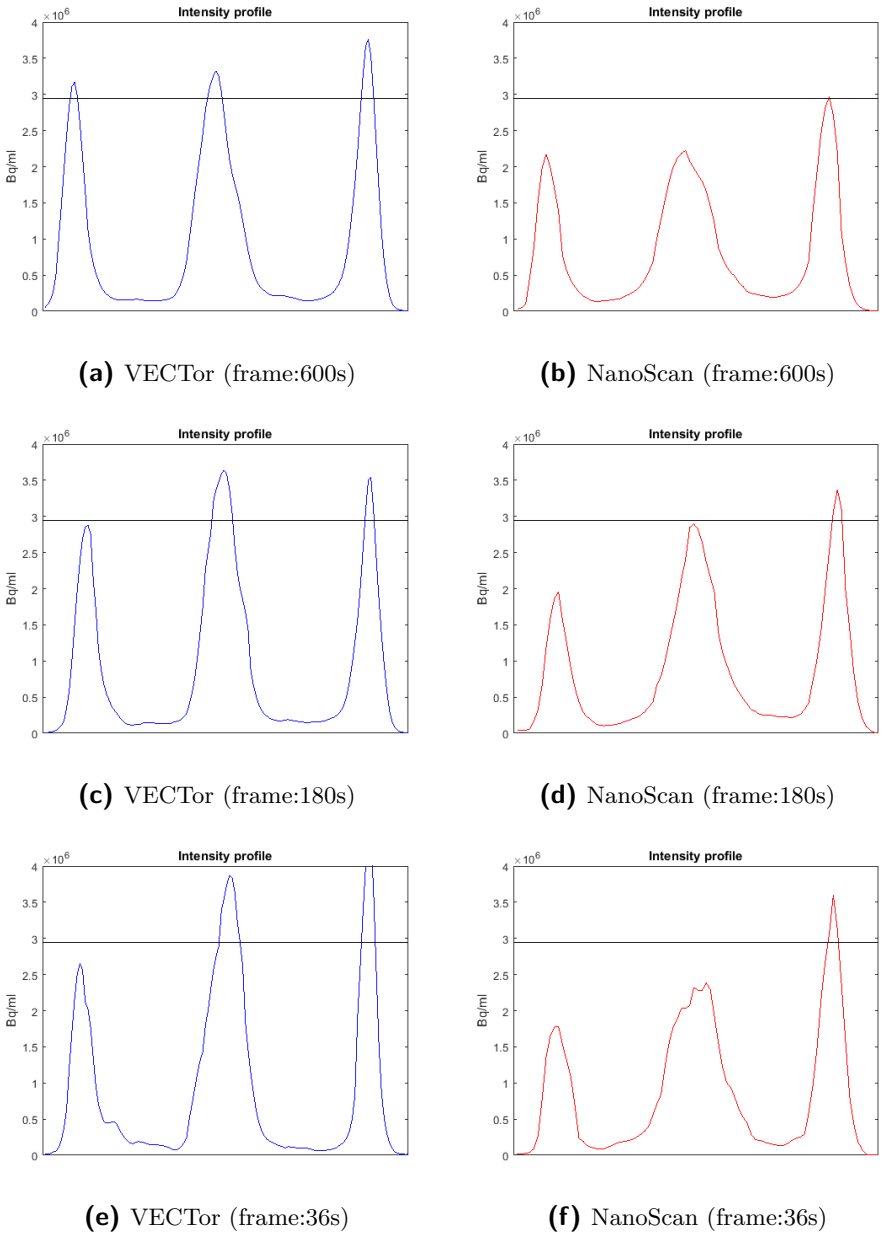

(a) VECTor (frame:600s) **(b)** NanoScan (frame:600s)

(c) VECTor (frame:180s) **(d)** NanoScan (frame:180s)

(e) VECTor (frame:36s) **(f)** NanoScan (frame:36s)

Figure 3-12: Intensity profiles through the reconstructed volumes of the cold compartments section of the SPECTIQ phantom acquired with VECTor (a,c,e) and NanoScan (b,d,f). SORs appear to be lower in the image acquired with VECTor.

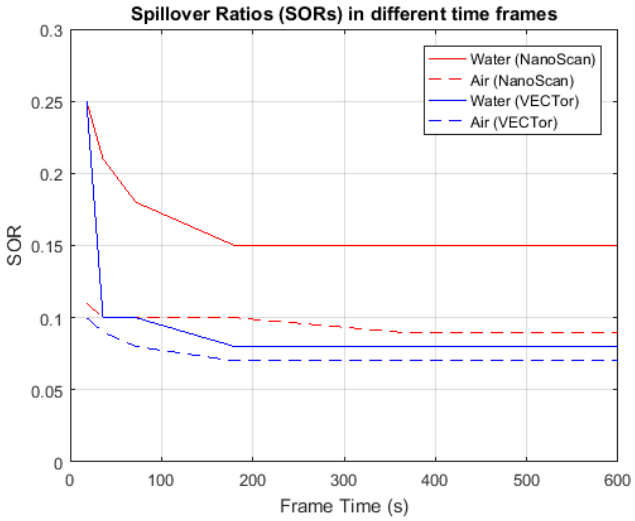

Figure 3-13: SORs of the cold water- and air-filled chambers of SPECTIQ phantom as a function of frame time. After a steep decline of the SORs when moving from the 18s to the 36s frame they start reaching convergence. The spillover ratio in the water compartment is approximately 46.6% lower in VECTor than in NanoScan. In addition, the spillover ratio in the air-filled compartment is also lower in VECTor (approximately 22.2%).

Chapter 4

Discussion & Conclusion

The performance of two preclinical imaging SPECT systems was evaluated for short frames imaging (ranging from a few seconds up to 600s duration). Therefore, our interest was oriented towards high-sensitivity SPECT scans in order to detect as many photons as possible in these time intervals. For the purposes of our experiments both imaging systems were equipped with high sensitivity collimator apertures. Before comparing the systems performances, experiments were conducted in order to assess the quantification accuracy of NanoScan and to select preferable fast imaging mode for the systems comparison. All acquisition parameters for all measurements were kept as equal as possible. The reconstruction parameters were chosen based on the recommended parameters of the systems software and regular users' experience with these systems.

4-1 Quantification Accuracy (NanoScan)

Visual evaluation of the syringes images showed strong spatial distortion at their edges when imaging with the stationary mode. The artifacts become less pronounced when performing imaging with the semi-stationary modes. This indicates a minimum of two detector positions (projections) is required in order to avoid distinct image artifacts due to angular undersampling. The effect of angular undersampling in images spatial distortion is in agreement with the study conducted by Lange et al (15).

In addition the syringes studies showed the ability of NanoScan to perform accurate activity recovery (up to 5% deviation from the dose calibrator measurement) for short frame times (6-30s).

The image noise analysis showed that the increase of frame duration results in images with lower noise. Furthermore, the noise in the images tends to decrease as the angular sampling increases. The same trend between noise and frame duration was observed in previous study (15).

4-2 Fast Imaging Mode Selection

Strong spatial distortion was observed at the rods of the NU4IQ phantom when using the stationary mode (Figure 3-4). The rods are depicted as triangular-shaped structures. The artifacts partially faded when the angular sampling was increased.

The comparison between the fast imaging modes of NanoScan showed that Semi-3 appears to provide more accurate activity recovery in small structures (less than 2mm diameter) than stationary and Semi-2 modes. However, the difference is significant only in the case of the 2mm diameter rod and the 30s frame.

Lower noise (experiment 2-4-1) and better activity recovery in small structures (experiment 2-4-2) in combination with the presence of less artifacts led to the selection of Semi-3 imaging mode for the comparison study of the two systems.

Despite the fact that the Semi-3 mode was selected as an optimal mode out of the three, for fast imaging, both stationary and Semi-2 modes can be used to recover activity from larger structures. In this way, the scan times can be reduced based on the demands of the imaging task.

4-3 Systems Comparison

Uniform Region of SPECTIQ phantom

The comparison study showed both systems have the ability to quantify radioactivity accurately in the uniform phantom section (21mm active diameter). NanoScan provided activity recovery with up to 5% overestimation (18s WB frame). This deviation from the ground truth value ($RC_{unif} = 1$) is acceptable (RC $\leq$ 5%). The RC in the uniform region remained almost stable in the case of VECTor (up to 5% deviation in activity recovery).

The noise in the images is reduced as the frame time (acquisition time) increases. The images acquired with the VECTor appear to have higher noise. A possible explanation is the size of the voxels that constitute the images. The voxels size in VECTor images are smaller (0.168mm) than the ones in the NanoScan images (0.258mm). When using smaller size voxels, less counts are allocated on each voxel resulting in higher noise levels. According to a study conducted by Budinger et al. (38) larger voxels contribute to lower noise in SPECT images. It should be noted that the voxel sizes were selected to be as similar as possible in terms of size. Another possible explanation is the number of iterations used could be large for so low count statistics resulting in over-iteration and higher noise levels (29). Variations in post-reconstruction filtering should be tested in order to help suppressing the noise and simultaneously preserve image quality (39).

Rods section of SPECTIQ phantom

The comparison between the two systems for activity recovery in the rods of SPECTIQ phantom showed VECTor appears to provide higher activity recovery in the three largest rods of the SPECTIQ phantom. However, the differences cannot be considered significant when the frame time is decreased (Figure 3-10).

The performance of VECTor in this task can be improved by focusing only on rods scan rather than a whole-body scan. In this way, the image quality can be improved, by reducing the number of bed positions. The possibility of performing dynamic SPECT with 15s whole-body frames and 1s single bed position frame has already been reported (14, 16).

Cold Compartmens section of SPECTIQ phantom

Spillover Ratios (SORs) have been mainly utilized in the evaluation of the scatter correction performance and has been investigated as a function of the number of iterations used during image reconstruction (27, 28). However, the spillover effect has not been investigated in literature based on acquisition time variations.

The spillover effect in the reconstructed images for both systems was not affected by the acquisition time frame used. The increase of the acquisition time tends to provide images where the spillover effect is reduced. There is a steep decline of the SORs between the 18s to the 36s frames which illustrates the spillover enhancement as the frame duration is reduced. It is observed for both systems that SOR_{wat} is larger than SOR_{air}, which is clearly expected because photon scatter is stronger in water than in air. In figure 3-13, it is clearly observed that the spillover in both cold phantom chambers is lower in VECTor than in NanoScan (approximately 46.6% and 22.2% in the water- and air-filled chambers respectively when they reach convergence).

4-4 General Remarks

It was not the aim of this study to fully optimize all acquisition and reconstruction parameters available for the two systems. For this purpose, additional settings should be taken into consideration including: activity used, post-reconstruction filtering variations, number of iterations and subsets.

There was large variation in literature about the amounts of activity used in (fast) imaging studies for both phantom and animal experiments (14–16). Therefore, there was no specific approach regarding the amounts of activity used in the present study. In some of the experiments the amount of the activity employed was high (eg. 10MBq/ml, 55MBq/ml). This condition is undesirable when conducting animal experiments because of the high radiation dose received by the subject. However, the potential of the systems to have the same performance in activity recovery for lower amounts of activity (eg. 3 MBq/ml) was proven in the SPECTIQ phantom experiment.

Standard reconstruction parameters were employed in this study (either default settings or regular users' preferences). Further investigation is needed in order to test if the applied combinations of subsets and iterations were enough to fully recover activity in the structures used in the experiments or if they have already led to convergence.

Using the NEMA standards as a measurement approach in experiments 2-4-2 and 2-4-3, an overestimation in activity recovery has been noticed in the phantoms rods. Activity recovery using maximum intensity values are usually overestimated because of statistical noise (34). This results in recovery coefficients larger than 1. This effect could possibly be attributed to an overshoot at the edges, known as Gibbs effect (40).

4-5 Conclusion

The performances of two preclinical SPECT systems (NanoScan, VECTor) for short time acquisitions were compared. The conducted experiments showed that the systems perform equally when conducting short frames imaging. Furthermore, the fast imaging mode of NanoScan employing three detector positions showed better performance than the other two fast imaging modes of this system.

Appendix A

Quantification Accuracy - NanoScan

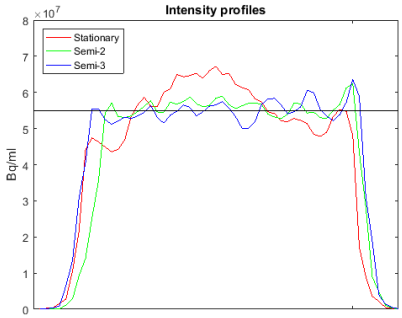

(a) 24s

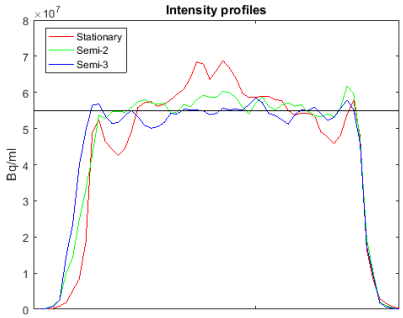

(b) 18s

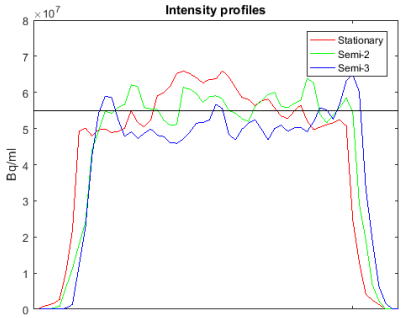

(c) 12s

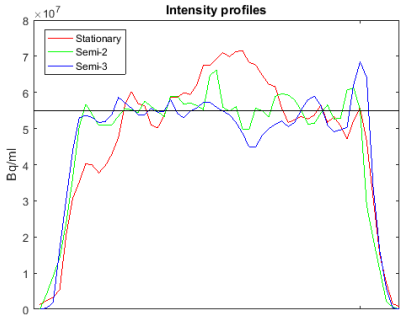

(d) 6s

Figure A-1: Intensity profiles drawn through the reconstructed syringes volumes for all time frames and imaging modes used.

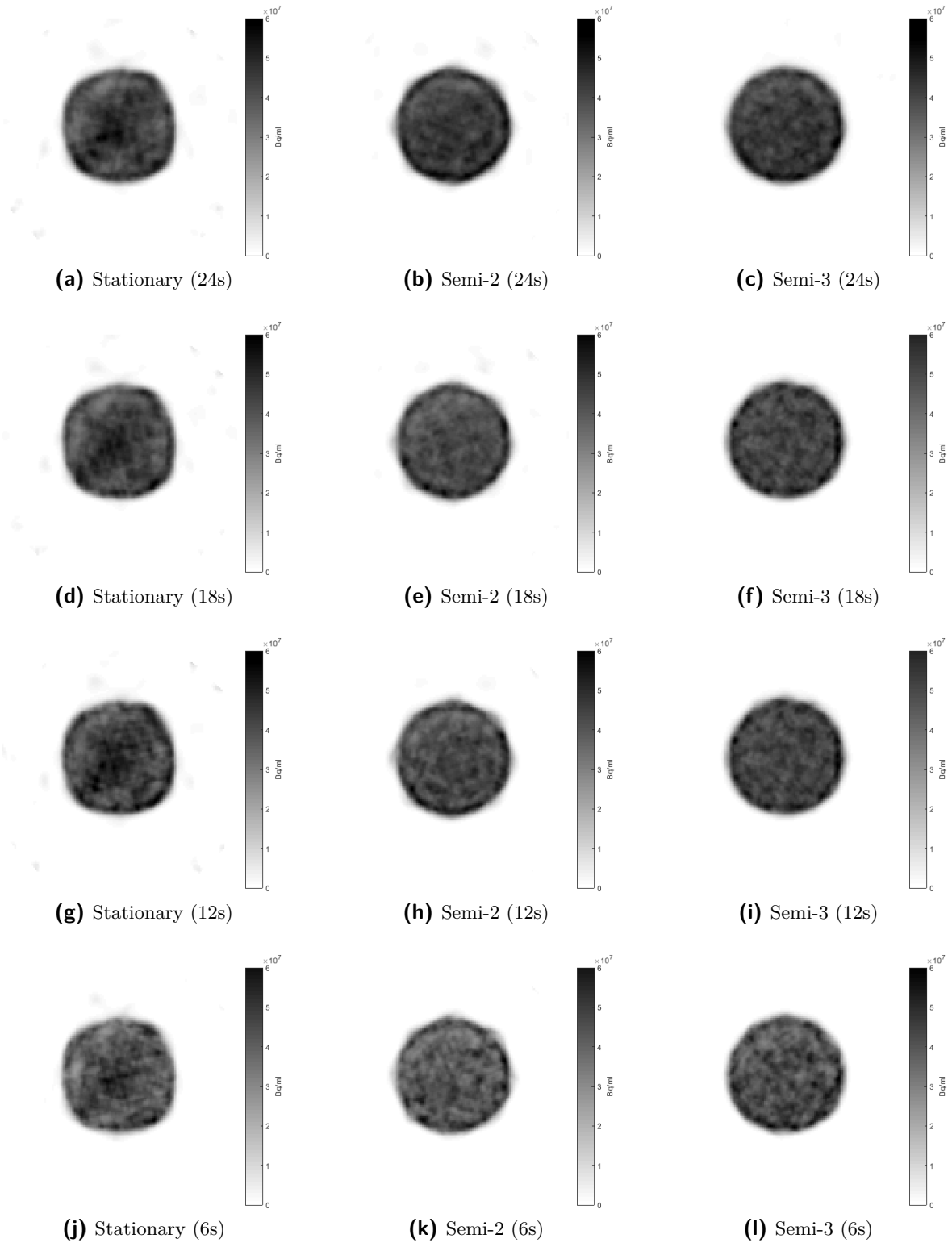

(a) Stationary (24s) **(b)** Semi-2 (24s) **(c)** Semi-3 (24s)

(d) Stationary (18s) **(e)** Semi-2 (18s) **(f)** Semi-3 (18s)

(g) Stationary (12s) **(h)** Semi-2 (12s) **(i)** Semi-3 (12s)

(j) Stationary (6s) **(k)** Semi-2 (6s) **(l)** Semi-3 (6s)

Figure A-2: Reconstructed transaxial slices of a 10ml syringe acquired with different time frames and different acquisition modes

Appendix B

Fast Imaging Mode Selection

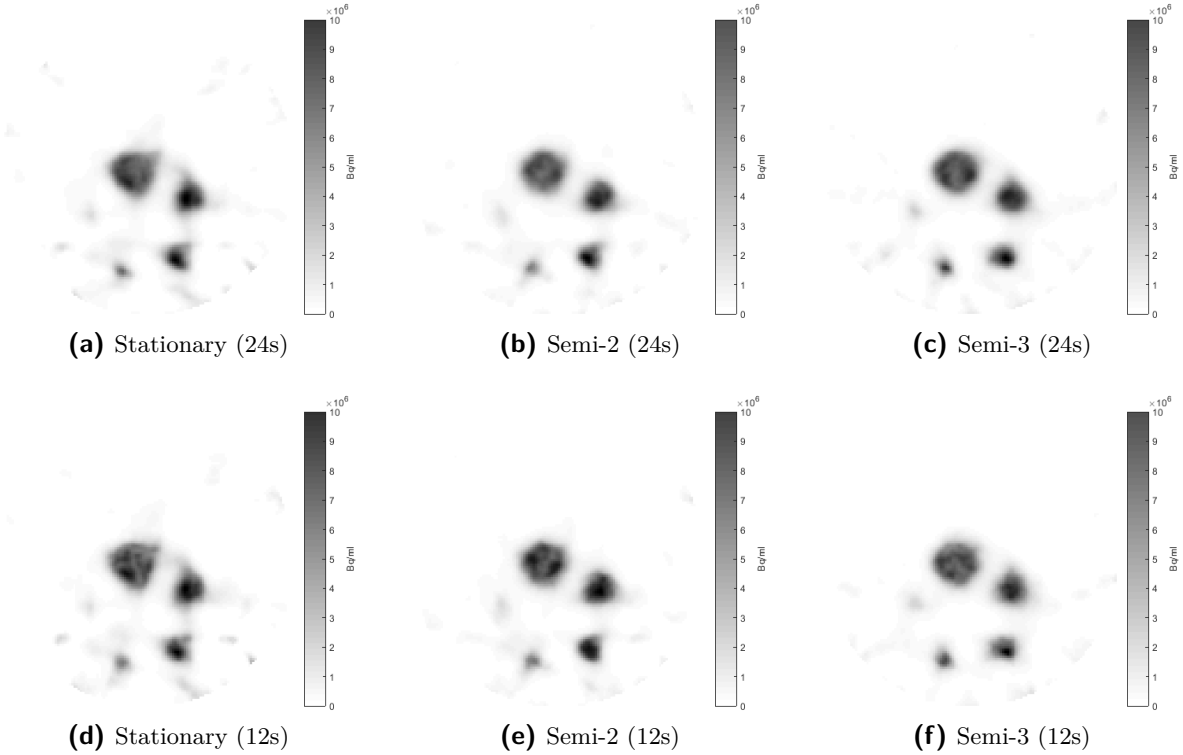

(a) Stationary (24s) **(b)** Semi-2 (24s) **(c)** Semi-3 (24s)

(d) Stationary (12s) **(e)** Semi-2 (12s) **(f)** Semi-3 (12s)

Figure B-1: Reconstructed transaxial slices of the NU4IQ phantom acquired with all fast imaging modes and two different frames (12,24s). Starting from the top rod and moving clockwise, the rods diameters are: 5,4,3,2 and 1mm

Appendix C

Systems Comparison Experiment

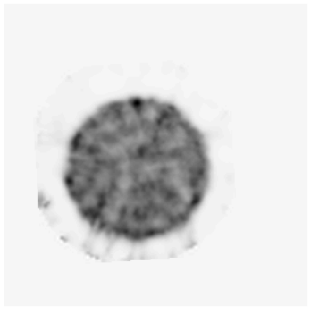

(a) VECTor (360s)

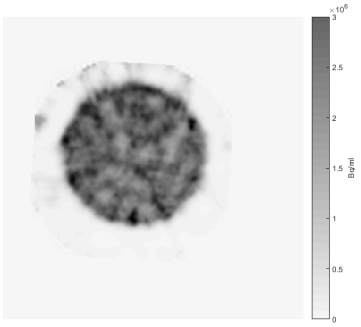

(b) VECTor (180s)

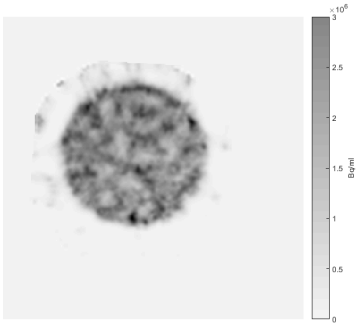

(c) VECTor (72s)

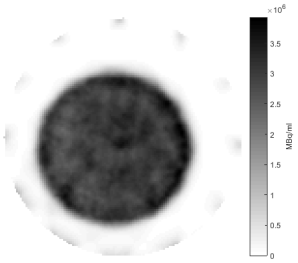

(d) NanoScan (360s)

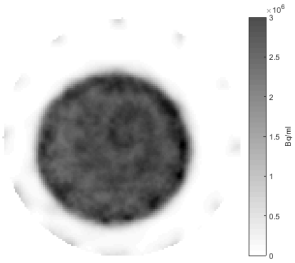

(e) NanoScan (180s)

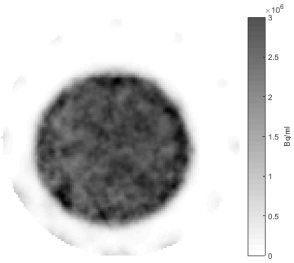

(f) NanoScan (72s)

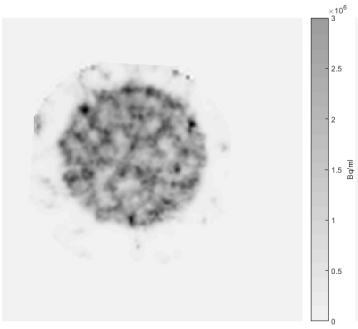

(g) VECTor (36s)

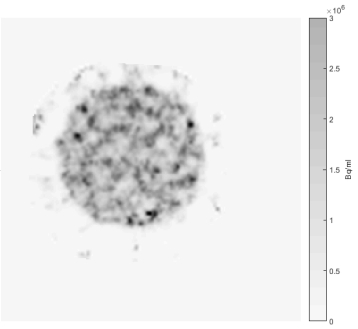

(h) VECTor (18s)

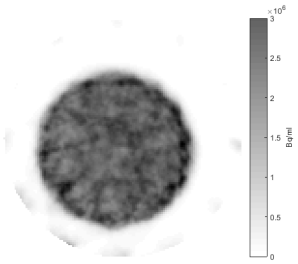

(i) NanoScan (36s)

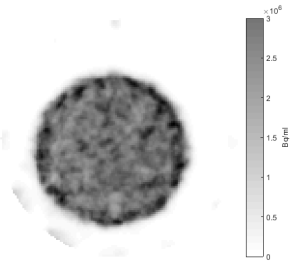

(j) NanoScan (18s)

Figure C-1: Reconstructed transaxial slices of the unifrom region of SPECTIQ phantom.

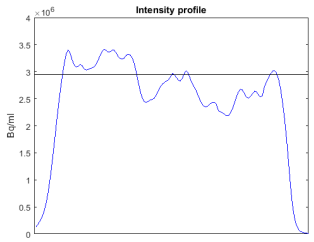

(a) VECTor (360s)

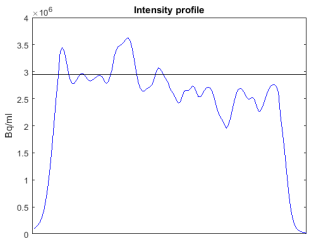

(b) VECTor (180s)

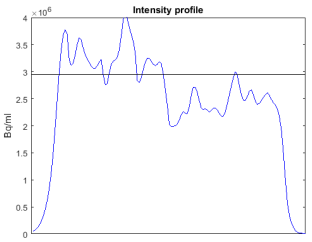

(c) VECTor (72s)

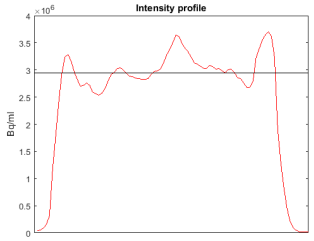

(d) NanoScan (360s)

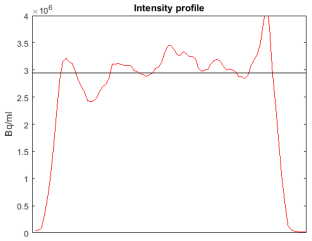

(e) NanoScan (180s)

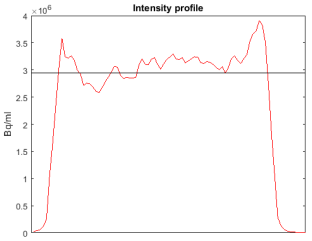

(f) NanoScan (72s)

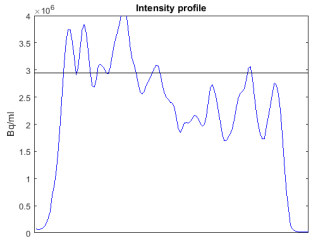

(g) VECTor (36s)

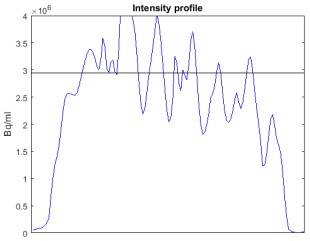

(h) VECTor (18s)

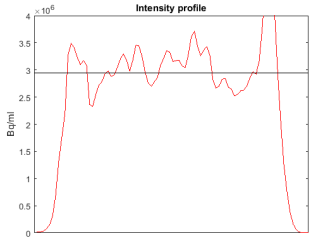

(i) NanoScan (36s)

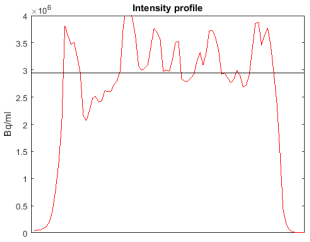

(j) NanoScan (18s)

Figure C-2: Intensity profiles drawn along the reconstructed slices of the unifrom region

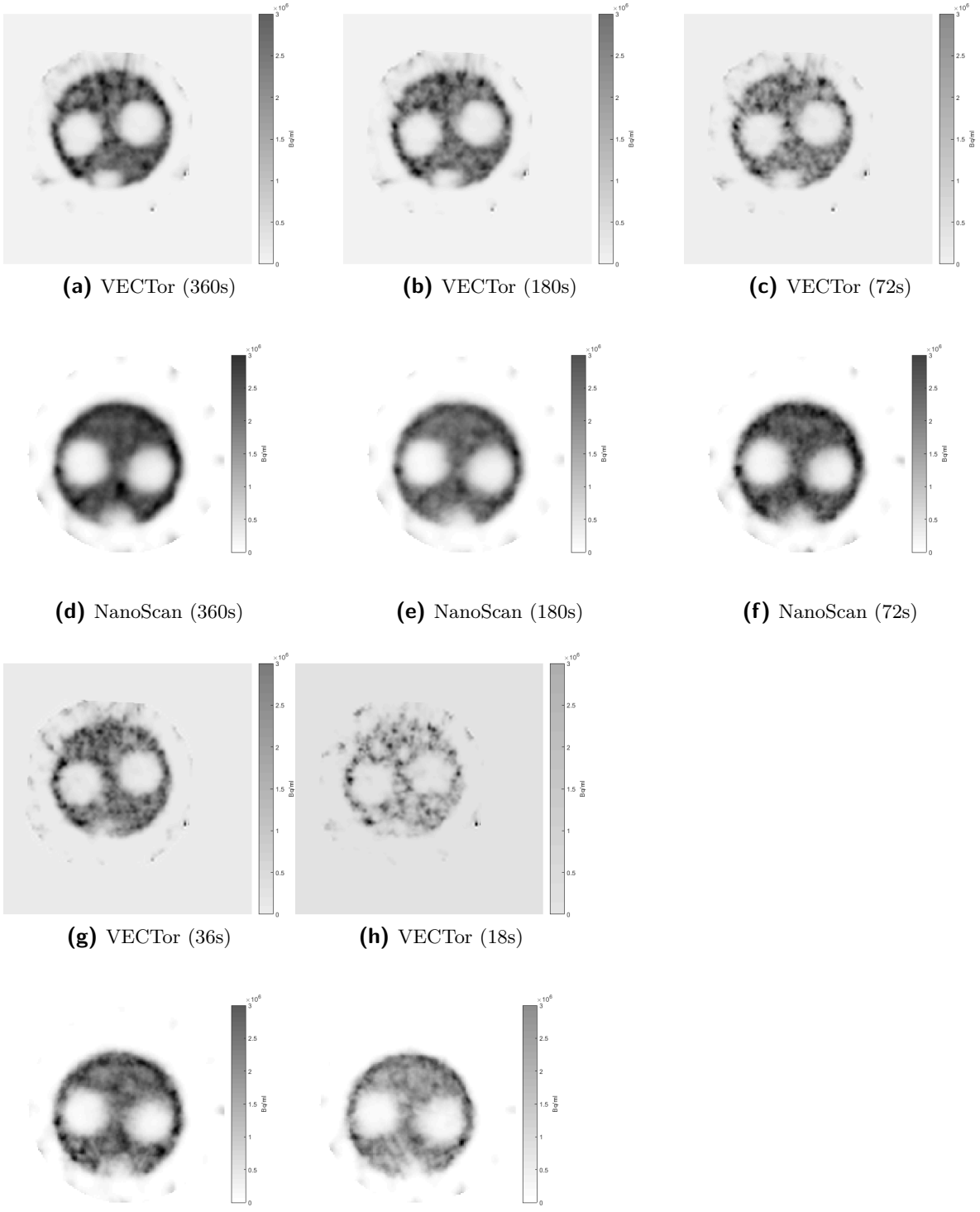

(a) VECTor (360s) **(b)** VECTor (180s) **(c)** VECTor (72s)

(d) NanoScan (360s) **(e)** NanoScan (180s) **(f)** NanoScan (72s)

(g) VECTor (36s) **(h)** VECTor (18s)

(i) NanoScan (36s) **(j)** NanoScan (18s)

Figure C-3: Reconstructed transaxial slices of the cold compartments section of SPECTIQ phantom.

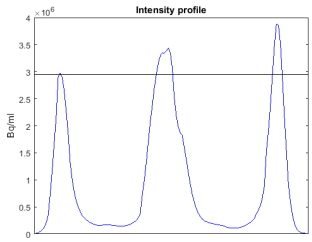

(a) VECTor (360s)

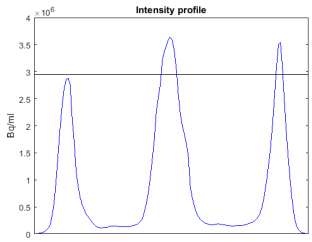

(b) VECTor (180s)

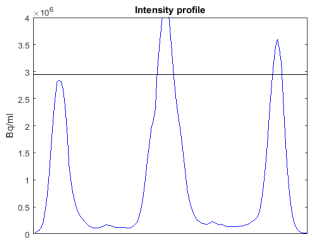

(c) VECTor (72s)

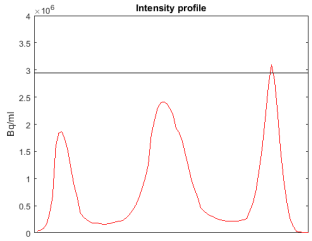

(d) NanoScan (360s)

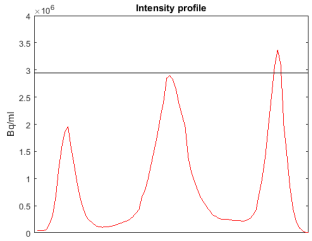

(e) NanoScan (180s)

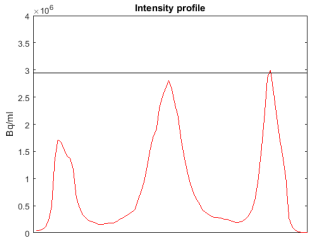

(f) NanoScan (72s)

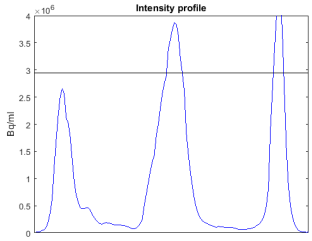

(g) VECTor (36s)

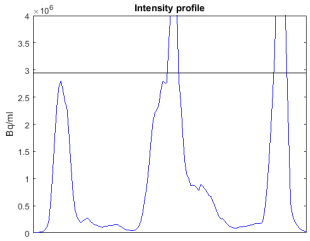

(h) VECTor (18s)

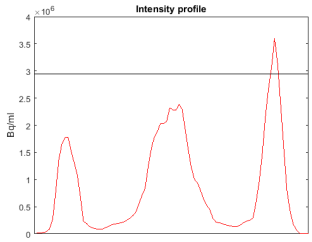

(i) NanoScan (36s)

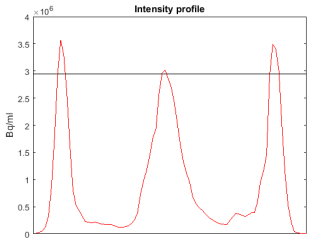

(j) NanoScan (18s)

Figure C-4: Intensity profiles drawn along the reconstructed slices of the cold compartments section

Bibliography

[1] Steven R Meikle, Peter Kench, Michael Kassiou, and Richard B Banati. Small animal SPECT and its place in the matrix of molecular imaging technologies. *Phys. Med. Biol*, 50(2005):45–61, 2005.

[2] Ciara M Finucane, Iain Murray, Jane K Sosabowski, Julie M Foster, and Stephen J Mather. Quantitative Accuracy of Low-Count SPECT Imaging in Phantom and In Vivo Mouse Studies. *International journal of molecular imaging*, 2011:197381, 2011.

[3] M. C. Goorden, F. van der Have, R. Kreuger, R. M. Ramakers, B. Vastenhouw, J. P. H. Burbach, J. Booij, C. F. M. Molthoff, and F. J. Beekman. VECTor: A Preclinical Imaging System for Simultaneous Submillimeter SPECT and PET. *Journal of Nuclear Medicine*, 54(2):306–313, 2012.

[4] M. Melis, R. Valkema, E. P. Krenning, and M. de Jong. Reduction of Renal Uptake of Radiolabeled Octreotate by Amifostine Coadministration. *Journal of Nuclear Medicine*, 53:749–753, 2012.

[5] Benjamin L Franc, Paul D Acton, Carina Mari, and Bruce H Hasegawa. Small-animal SPECT and SPECT/CT: important tools for preclinical investigation. *Journal of nuclear medicine : official publication, Society of Nuclear Medicine*, 49(10):1651–1663, 2008.

[6] Shankar Vallabhajosula. *Molecular imaging: Radiopharmaceuticals for PET and SPECT*. 2009.

[7] Robert a de Kemp, Frederick H Epstein, Ciprian Catana, Benjamin M W Tsui, and Erik L Ritman. Small-animal molecular imaging methods. *The Journal of Nuclear Medicine*, 51(5):18S–32S, 2010.

[8] Reza Golestani, Chao Wu, René A. Tio, Clark J. Zeebregts, Artiom D. Petrov, Freek J. Beekman, Rudi A J O Dierckx, Hendrikus H. Boersma, and Riemer H J A Slart. Small-animal SPECT and SPECT/CT: Application in cardiovascular research, 2010.

[9] Anders Kielland and Harald Carlsen. Molecular imaging of transcriptional regulation during inflammation. *Journal of inflammation (London, England)*, 7:20, 2010.

[10] Anna J Studwell and Darrell N Kotton. A Shift From Cell Cultures to Creatures: In Vivo Imaging of Small Animals in Experimental Regenerative Medicine. *Molecular Therapy*, 19(11):1933–1941, 2011.

[11] Sara Neyt, Maarten T Huisman, Christian Vanhove, Hilde De Man, Maarten Vliegen, Lieselotte Moerman, Caroline Dumolyn, Geert Mannens, and Filip De Vos. In vivo visualization and quantification of (Disturbed) Oatp-mediated hepatic uptake and Mrp2-mediated biliary excretion of 99mTc-mebrofenin in mice. *Journal of nuclear medicine : official publication, Society of Nuclear Medicine*, 54(4):624–30, 2013.

[12] Monique R. Bernsen, Pieter E B Vaissier, Roel Van Holen, Jan Booij, Freek J. Beekman, and Marion De Jong. The role of Preclinical SPECT in oncological and neurological research in combination with either CT or MRI, 2014.

[13] B Vastenhouw, F Van Der Have, AJA Van Der Linden, L Von Oerthel, J Booij, JPH Burbach, MP Smidt, and FJ Beekman. Movies of dopamine transporter occupancy with ultra-high resolution focusing pinhole spect. *Molecular psychiatry*, 12(11):984–987, 2007.

[14] Pieter EB Vaissier, Marlies C Goorden, Brendan Vastenhouw, Frans van der Have, Ruud M Ramakers, and Freek J Beekman. Fast spiral SPECT with stationary γ-cameras and focusing pinholes. *Journal of Nuclear Medicine*, 53(8):1292–9, 2012.

[15] Catharina Lange, Ivayla Apostolova, Mathias Lukas, Kai P. Huang, Frank Hofheinz, Betina Gregor-Mamoudou, Winfried Brenner, and Ralph Buchert. Performance evaluation of stationary and semi-stationary acquisition with a non-stationary small animal multi-pinhole SPECT system. *Molecular Imaging and Biology*, 16(3):311–316, 2014.

[16] O. Ivashchenko, F. van der Have, M. C. Goorden, R. M. Ramakers, and F. J. Beekman. Ultra-High-Sensitivity Submillimeter Mouse SPECT. *Journal of Nuclear Medicine*, 56(3):470–475, 2015.

[17] Frans van der Have, Oleksandra Ivashchenko, Marlies C Goorden, Ruud M Ramakers, and Freek J Beekman. High-resolution clustered pinhole 131 iodine spect imaging in mice. *Nuclear medicine and biology*, 43(8):506–511, 2016.

[18] George N Sfakianakis and Mike F Georgiou. Mag3 spect: a rapid procedure to evaluate the renal parenchyma. *The Journal of Nuclear Medicine*, 38(3):478, 1997.

[19] Marleen Melis, Jan de Swart, Monique de Visser, Saskia C Berndsen, Stuart Koelewijn, Roelf Valkema, Otto C Boerman, Eric P Krenning, and Marion de Jong. Dynamic and static small-animal spect in rats for monitoring renal function after 177lu-labeled tyr3-octreotate radionuclide therapy. *Journal of nuclear medicine*, 51(12):1962–1968, 2010.

[20] Isky Gordon, Amy Piepsz, and Rune Sixt. Guidelines for standard and diuretic renogram in children. *European journal of nuclear medicine and molecular imaging*, 38(6):1175–1188, 2011.

[21] WP Klein, HH Barrett, IW Pang, DD Patton, MM Rogulski, JD Sain, and WE Smith. Fastspect: electrical and mechanical design of a high-resolution dynamic spect imager. In *Nuclear Science Symposium and Medical Imaging Conference Record, 1995., 1995 IEEE*, volume 2, pages 931–933. IEEE, 1995.

[22] Lars R. Furenlid, Donald W. Wilson, Yi Chun Chen, Hyunki Kim, Philip J. Pietraski, Michael J. Crawford, and Harrison H. Barrett. FastSPECT II: A second-generation high-resolution dynamic SPECT imager. *IEEE Transactions on Nuclear Science*, 51(3 II):631–635, 2004.

[23] Freek J. Beekman, Frans van der Have, Brendan Vastenhouw, Annemarie J.A. van der Linden, Peter P. van Rijk, J. Peter H. Burbach, and Marten P. Smidt. U-SPECT-I: A Novel System for Submillimeter-Resolution Tomography with Radiolabeled Molecules in Mice. *J. Nucl. Med.*, 46(7):1194–1200, jul 2005.

[24] Frans van der Have, Brendan Vastenhouw, Ruud M Ramakers, Woutjan Branderhorst, Jens O Krah, Changguo Ji, Steven G Staelens, and Freek J Beekman. U-SPECT-II: An Ultra-High-Resolution Device for Molecular Small-Animal Imaging. *Journal of nuclear medicine : official publication, Society of Nuclear Medicine*, 50(4):599–605, 2009.

[25] Woutjan Branderhorst, Brendan Vastenhouw, Frans Van Der Have, Erwin L A Blezer, Wim K. Bleeker, and Freek J. Beekman. Targeted multi-pinhole SPECT. *European Journal of Nuclear Medicine and Molecular Imaging*, 38(3):552–561, 2011.

[26] Jan de Swart, Ho Sze Chan, Marlies C Goorden, Alfred Morgenstern, Frank Bruchertseifer, Freek J Beekman, Marion de Jong, and Mark W Konijnenberg. Utilizing High-Energy γ-Photons for High-Resolution 213Bi SPECT in Mice. *Journal of nuclear medicine : official publication, Society of Nuclear Medicine*, 57(3):486–92, 2016.

[27] a. a. Harteveld, a. P. W. Meeuwis, J. a. Disselhorst, C. H. Slump, W. J. G. Oyen, O. C. Boerman, and E. P. Visser. Using the NEMA NU 4 PET Image Quality Phantom in Multipinhole Small-Animal SPECT. *Journal of Nuclear Medicine*, 52(10):1646–1653, 2011.

[28] Eric P. Visser, Anita A. Harteveld, Antoi P W Meeuwis, Jonathan A. Disselhorst, Freek J. Beekman, Wim J G Oyen, and Otto C. Boerman. Image quality phantom and parameters for high spatial resolution small-animal SPECT. *Nuclear Instruments and Methods in Physics Research, Section A: Accelerators, Spectrometers, Detectors and Associated Equipment*, 654(1):539–545, 2011.

[29] Frederic Boisson, David Zahra, Arvind Parmar, Marie-Claude Gregoire, Steven R Meikle, Hasar Hamse, and Anthonin Reilhac. Imaging capabilities of the Inveon SPECT system using single-and multipinhole collimators. *Journal of Nuclear Medicine*, 54:1833–40, 2013.

[30] APW Meeuwis, F van der Have, FJ Beekman, WJG Oyen, OC Boerman, and EP Visser. Image quality of u-spect-ii collimators using an adapted nema phantom. In *EUROPEAN JOURNAL OF NUCLEAR MEDICINE AND MOLECULAR IMAGING*, volume 39, pages S289–S289. SPRINGER 233 SPRING ST, NEW YORK, NY 10013 USA, 2012.

[31] NEMA Standards Publication NU 4-2008: Performance Measurements of Small Animal Positron Emission Tomographs, 2008.

[32] Jonathan a Disselhorst, Maarten Brom, Peter Laverman, Cornelius H Slump, Otto C Boerman, Wim J G Oyen, Martin Gotthardt, and Eric P Visser. Image-quality assessment for several positron emitters using the NEMA NU 4-2008 standards in the Siemens

Inveon small-animal PET scanner. *Journal of nuclear medicine : official publication, Society of Nuclear Medicine*, 51(4):610–617, 2010.

[33] Andrew L Goertzen, Qinan Bao, Mélanie Bergeron, Eric Blankemeyer, Stephan Blinder, Mario Cañadas, Arion F Chatziioannou, Katherine Dinelle, Esmat Elhami, Hans-Sonke Jans, et al. Nema nu 4-2008 comparison of preclinical pet imaging systems. *Journal of Nuclear Medicine*, 53(8):1300–1309, 2012.

[34] Keiichi Magota, Naoki Kubo, Yuji Kuge, Ken Ichi Nishijima, Songji Zhao, and Nagara Tamaki. Performance characterization of the Inveon preclinical small-animal PET/SPECT/CT system for multimodality imaging. *European Journal of Nuclear Medicine and Molecular Imaging*, 38(4):742–752, 2011.

[35] Steven Deleye, Roel Van Holen, Jeroen Verhaeghe, Stefaan Vandenberghe, Sigrid Stroobants, and Steven Staelens. Performance evaluation of small-animal multipinhole ??sPECT scanners for mouse imaging. *European Journal of Nuclear Medicine and Molecular Imaging*, 40(5):744–758, 2013.

[36] Kenneth Lange and Richard Carson. EM Reconstruction Algorithms for Emission and Transmission Tomography. *Journal of Computer Assisted Tomography*, 8(2):306–316, 1984.

[37] Woutjan Branderhorst, Brendan Vastenhouw, and Freek J Beekman. Pixel-based subsets for rapid multi-pinhole spect reconstruction. *Physics in medicine and biology*, 55(7):2023, 2010.

[38] Thomas F Budinger. Physical attributes of single-photon tomography. *Journal of nuclear medicine: official publication, Society of Nuclear Medicine*, 21(6):579–592, 1980.

[39] Maria Lyra and Agapi Ploussi. Filtering in spect image reconstruction. *Journal of Biomedical Imaging*, 2011:10, 2011.

[40] Donald L Snyder, Michael I Miller, Lewis J Thomas, and David G Politte. Noise and edge artifacts in maximum-likelihood reconstructions for emission tomography. *IEEE transactions on medical imaging*, 6(3):228–238, 1987.